

To my mother and my father...

INDEX

FIGURE INDEX	4
TABLE INDEX.....	7
CHAPTER 1 - INTRODUCTION.....	8
1.1 Overview on the directional stability and scope of the work	8
1.2 Advantages of a modular model	16
1.3 The problem of the minimum control speed.....	18
CHAPTER 2 - THE EXPERIMENTAL MODULAR MODEL	22
2.1 Introduction to the model.....	22
2.2 Wing.....	26
2.3 Fuselage nose	26
2.4 Fuselage cabin.....	28
2.5 Vertical tail	28
2.6 Fuselage tail-cone	30
2.7 Horizontal tail	32
2.8 Other small components	32
CHAPTER 3 - APPROACH TO WIND TUNNEL TESTING	34
3.1 Introduction.....	34
3.2 Wind tunnel of the DII.....	36
3.3 Instrumentation	39
3.3.1 Measurement instrumentation.....	39
3.3.2 Control instrumentation	42
3.3.3 Acquisition and elaboration	42
3.4 Setup issues.....	44

3.4.1 Center of gravity location	44
3.4.2 Stiffening of the sting	45
3.5 Setup of the wind tunnel	47
3.5.1 Verification of the balance readings	47
3.5.2 Scale effect and trip strips.....	50
3.6 Wind tunnel corrections.....	51
CHAPTER 4 - WIND TUNNEL TESTS	53
4.1 Reference system	53
4.2 Test procedure.....	54
4.1.1 Setup of the configuration.....	54
4.1.2 Data acquisition	54
4.1.3 Data elaboration and storage.....	55
4.3 The experimental tests campaign.....	57
4.3.1 Preliminary tests	57
4.3.2 Configurations results	58
4.3.3 Mutual aerodynamic interference effect	69
REFERENCES.....	77
ACKNOWLEDGEMENT/RINGRAZIAMENTI	78

FIGURE INDEX

Fig 1. 1 – Asymmetric flight notation and the straight slip	8
Fig 1. 2 – A body of revolution in potential flow t angle of attack	11
Fig 1. 3 – Yawing moment of vertical tail	11
Fig 1. 4 - Principal geometric parameter	12
Fig 1. 5 – Typical regional turboprop aircraft	15
Fig 1. 6 – Layout of configurations investigated	16
Fig 1. 7 – Some configurations	17
Fig 1. 8 – Example of aircraft vertical tail	18
Fig 1. 9 – Most important forces and moments acting on the airplane while using the rudder to counteract the asymmetric thrust and while keeping the wing level.....	19
Fig 1. 10 – Yaw moment due to asymmetric power	20
Fig 1. 11 - Chart to preliminary select the vertical tail area S_v according to airborne minimum control speed limit.....	21
Fig 2. 1 – Model main dimensions (units in mm).....	23
Fig 2. 2 – Model exploded view. The markings correspond to the items of Tab 2.1	23
Fig 2. 3 – Sanded parts.....	25
Fig 2. 4 – Metals parts	25
Fig 2. 5 - Wing.....	25
Fig 2. 6 – Fuselage nose: (a) CAD image; (b) manufactured component	27
Fig 2. 7 – Fuselage cabin	27
Fig 2. 8 – Two covers Fig 2. 9 – Countersunk to keep wing in high/low position...	27
Fig 2. 10 - (a) Vertical tails comparison ($AR_v=1 - 1.5 - 2$); (b) Vertical plate.....	29
Fig 2. 11 – (a) Fuselage tail cones; (b) Sterns of the tail cones	29
Fig 2. 12 - (z_{fvc}/r_f) parameter	31
Fig 2. 13 – Vertical tail assembly with load cell	31
Fig 2. 14 – Loads path with the vertical tail load cell.....	31
Fig 2. 15 – Horizontal tail: (A) Body mounted; (B) Tail mounted.....	33
Fig 2. 16 – Covers aluminium sheets.....	33

Fig 2. 17 – Iron interface plate.....	33
Fig 2. 18 – Tail-cone stern fillet	33
Fig 3. 1 - Main subsonic wind tunnel facility	36
Fig 3. 2 - Plane form and geometric dimensions of the DII's wind tunnel facility ...	37
Fig 3. 3 - Lateral directional strain gage balance.....	40
Fig 3. 4 - The off-center load cell	40
Fig 3. 5 - Inclinator	40
Fig 3. 6 – Potentiometer.....	43
Fig 3. 7 – Sideslip mechanism.....	43
Fig 3. 8 – Spartan system 16 channels.....	43
Fig 3. 9 - Model with lead cylinder in the fuselage nose.....	46
Fig 3. 10 - Sting stiffened	46
Fig 3. 11 – Test of the off-center load cell.....	49
Fig 3. 12 – Flow visualization on vertical tail	49
Fig 3. 13 – Flow visualization on wing	49
Fig 4. 1 – Reference system.....	53
Fig 4. 2 – Location of the reference point.....	56
Fig 4. 3 – Preliminary tests (Trip strips).....	57
Fig 4. 4 – Positions of the horizontal plane.	59
Fig 4. 5 – BH_WH_V20_H5 configuration.....	59
Fig 4. 6 – a) BH; b) BH_V15; c) BH_V15_H1	62
Fig 4. 7 – CN versus β	63
Fig 4. 8 – CN_vertical versus β	63
Fig 4. 9 – Croll versus β	64
Fig 4. 10 - BH_WH_V15_H1	65
Fig 4. 11 - BH_WL_V15_H1	65
Fig 4. 12 – CN versus β for indicated configurations.....	66
Fig 4. 13 – CN_v for indicated configurations	66
Fig 4. 14 . Croll versus β for indicated configurations	67

Fig 4. 15 – Effect of wing position respect the fuselage in sideslip conditions.....	67
Fig 4. 16 – Effect of the wing position on the CN.....	68
Fig 4. 17 – Effect of the wing position on the Croll	68
Fig 4. 18 – BH_V10.....	69
Fig 4. 19 – BH_V15.....	69
Fig 4. 20 – BH_V20.....	70
Fig 4. 21 – CN_beta and Croll_beta versus ARv	71
Fig 4. 22 – Interference factors	71
Fig 4. 23 – b_v/d_{fv}	72
Fig 4. 24 – Lift curve slope of the isolated vertical tailplane	72
Fig 4. 25 – Example of WBV configuration with high wing	73
Fig 4. 26 – Example of WBV configuration with low wing.....	73
Fig 4. 27 – Effect wing position on $C_N\beta$	74
Fig 4. 28 - Effect wing position on $C_{N\beta v}$	74
Fig 4. 29 - $\left(\frac{z_h}{b_v}\right)$ parameter	75
Fig 4. 30 – Empennage configurations	75
Fig 4. 31 – Aerodynamic interference factor due to the horizontal stabilizer on the vertical tailplane. (High wing)	76
Fig 4. 32 – Aerodynamic interference factor due to the horizontal stabilizer on the vertical tailplane. (Low wing).....	76

TABLE INDEX

Tab. 1. 1 – Large turboprop aircraft main characteristics.....	14
Tab. 2. 1 – Bill of materials. Surface and volume are reported only for the machined components.	24
Tab. 2. 2 – Prolab 65 properties.....	24
Tab. 2. 3 - Wing’s characteristics	26
Tab. 2. 4 – Dimensions of the fuselage components	26
Tab. 2. 5 – Dimensions of the lifting surface of the model.	28
Tab 3. 1 – Wind tunnel of the DII, main characteristics.....	36
Tab 3. 2 - Estimation of pitching moment contributes of weight and lift.....	46

CHAPTER 1 - INTRODUCTION

1.1 OVERVIEW ON THE DIRECTIONAL STABILITY AND SCOPE OF THE WORK

In order to investigate the characteristics of an airplane it is necessary to consider the case when its flight path no longer lies in the plane of symmetry. This means that, as shown in Fig. 1.1, the relative wind will be making some angle to the airplane's center line. This angle is called the angle of sideslip β and it is assumed to be positive in sign when the relative wind strikes on the right of the pilot.

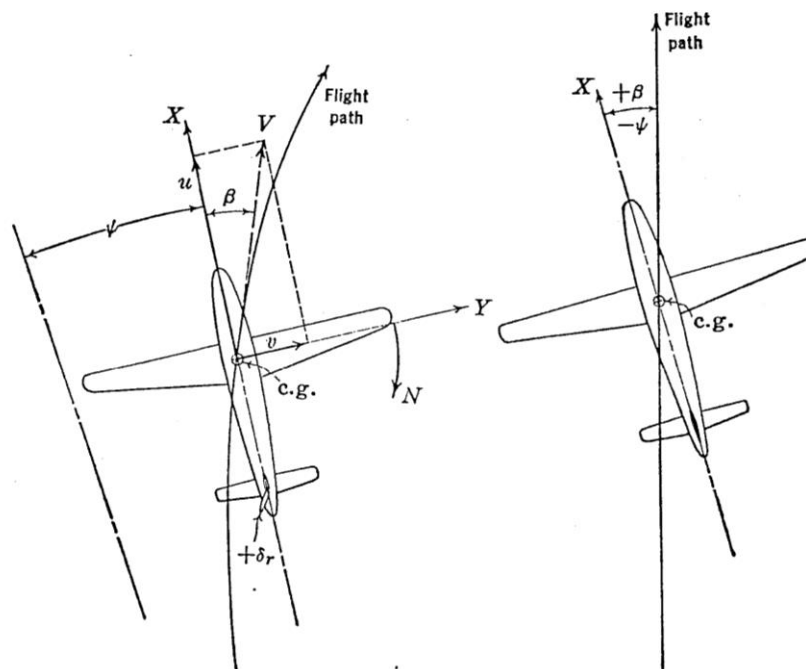


Fig 1. 1 – Asymmetric flight notation and the straight slip

The angle of sideslip, β , is equal to $\sin^{-1}(v/V)$ or for the small angles encountered in normal flight $\beta \cong (v/V)$. It should be noted that, for the curved flight paths shown, the angle of yaw, ψ , is defined as the angular displacement of the airplane's center line from some azimuth direction taken as zero at some given instant of time, and ψ does not equal β . For instance in a 360-degree turn the airplane has yawed 360

degrees, but may have had no sideslip during the entire maneuver. For sideslips during which a straight path is maintained, the angle of yaw, ψ , is equal in magnitude but opposite in sign to the angle of sideslip, β . Considerable confusion has arisen because of the misunderstanding of the terms yaw and sideslip. In most cases the term yaw is used to define the angle of the relative wind to the plane of symmetry, which although incorrect in certain phases of the problem is perfectly permissible if the straight flight path conditions are maintained (Ref. [1]).

The static directional stability of the airplane is its tendency to develop restoring moments when disturbed from its equilibrium angle of sideslip, usually taken as zero. The static problem, then, is the study of the airplane's yawing moments developed because of sideslip, to see if the yawing moment so developed will tend to reduce the sideslip or increase it. The static directional stability can be developed as was the static longitudinal stability, by summing up the stability contributions of the component parts of the airplane. Each of these components produces yawing moments when flying at angles of sideslip, and the study of the variation of the total yawing moment with angle of sideslip gives the magnitude of the directional stability.

As it has been done in all other phases of aerodynamics the yawing moment coefficient will be discussed instead of the dimensional yawing moment. The coefficient is obtained by dividing the yawing moment by the dynamic pressure q , the wing area S and the wing span b :

$$C_N = \frac{N}{q \cdot S \cdot b}$$

The directional stability of the airplane can be assessed if a curve of yawing moment coefficient C_N with β is obtained for any given airplane. A positive slope of this curve is required for static directional stability. The derivation $dC_N/d\beta$ will be given in the short-hand notation C_{N_β} and will be given per degree.

The desirable level of directional stability in terms of the criterion C_{N_β} , is very difficult to express in general terms. There have been practically no cases

reported of airplanes having too much directional stability. For normal airplane configurations directional stability levels of C_{N_β} between $.0015 \text{ deg}^{-1}$ and $.0020 \text{ deg}^{-1}$ have been considered good, with $C_{N_\beta} = 0.0005 \text{ deg}^{-1}$ a lower limit [1]. As mentioned above, in order to obtain the final variation analytically, the magnitude of the contributions from the major components must be developed analytically and then summed up.

In first approximation the aircraft yawing moment coefficient derivative due to sideslip can be calculated as follows

$$C_{N_\beta} = C_{N_{\beta v}} + C_{N_{\beta f}} + \text{minoreffects} \quad (1.1)$$

- It is interesting to note that the wing's contribution to directional stability is very small. The factor that affects the contribution of the wing is its angle of sweep Λ . A swept-back wings have slight directional stability, while swept-forward wings are slightly unstable. The wing contribution to directional stability is in many cases negligible in comparison to the contributions of the other parts of the airplane.
- The contribution of the fuselage to the directional stability of the airplane is usually unstable ($C_{N_{\beta f}} < 0$) and certainly one of the major effects. A physical explanation for this effect can be seen from Fig 1.2. Considering the fuselage to be represented by a body of revolution placed in a potential flow field the pressure distribution is roughly as indicated by the + and - signs in Figure. In potential flow, at a given angle of attack α , the following observations can be made: net pressure drag is zero, net lift is zero and net pitching moment is positive (Ref. [2]). As a consequence the fuselage will add a positively increasing pitching moment with each increase of angle of attack. This fuselage effect is also called the Munk effect (after its discoverer, Max Munk). According to Munk's theory the

moment created by the potential flow of an ideal fluid at an angle of attack is a function of the dynamic pressure q and of the volume of the fuselage. The yawing moment due to an angle of sideslip β is exactly the same. Several empirical approaches to the estimation of the isolated fuselage yawing moments have been made in the past.

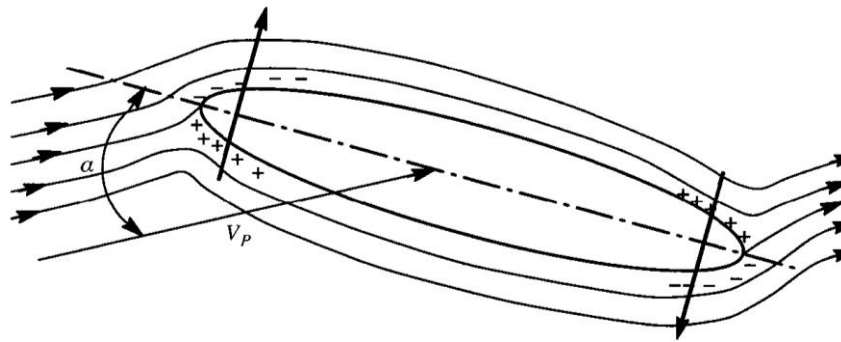


Fig 1. 2 – A body of revolution in potential flow t angle of attack

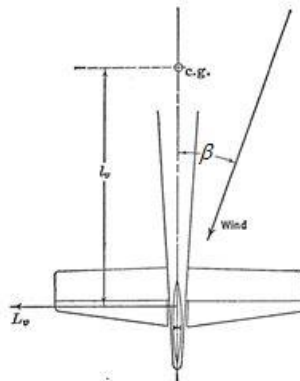


Fig 1. 3 – Yawing moment of vertical tail

- The vertical tail is thus necessary to overcome the instability of the fuselage and also to give the desired level of directional stability. The stability contribution of the isolated vertical tail can be computed as follows. The yawing moment produced by the vertical tail at some angle of sideslip can be considered simply as the lift created on the vertical tail, L_v , multiplied by the arm from the aerodynamic center of the vertical tail to the airplane's center of gravity, l_v (see Fig 1.3). It's clear that $C_{N_{\beta v}} > 0$ and much greater than zero as much as the vertical plane is located behind the center of gravity.

It's paramount now highlight that the directional stability of the combination of vertical tail plus fuselage is usually different from the sum of the two isolated components discussed so far. More generally, as it said also extends to the case of the complete aircraft configuration and it is due to the aerodynamic interference among all aircraft components.

In particular, our attention is focused on the vertical tail plane because it plays the role of the stabilizing surface. The aircraft directional stability provided by the vertical tail is influenced by:

- a. the fuselage cross-flow encountered in sideslip;
- b. the horizontal tail position and size;
- c. the wing-body wake and the sidewash effect.

a. Effect of the fuselage

A body in sideslip exhibits a flow characteristic similar to a cylinder in an airflow. For potential flow the peak local velocity occurs at the top at the cylinder and is equal to twice the free-stream cross-flow velocity. Actually, separation exists on the leeward side, reducing the peak velocity from the potential-flow value. Anyway, the velocity decays to the free-stream cross-flow value with distance from the body surface. Thus, tail-body combinations with large bodies and small tails have a greater effectiveness per unit area than combinations with large tails and small bodies and this trend is exhibited by test data. The fuselage directly alters the vertical tail incidence because of the cross-flow around the body. The principal geometric parameter governing this interference is the ratio of the vertical tail span b_v to fuselage height d_{fv} , representing the relative size between the vertical stabilizer and the fuselage section where the former is located.

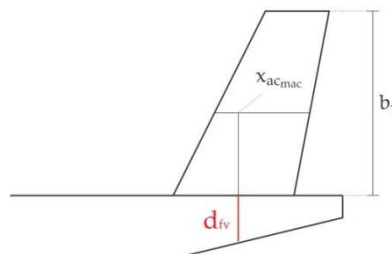


Fig 1. 4 - Principal geometric parameter

b. Effect of the horizontal plane

The presence of a horizontal panel in the vicinity of a vertical panel causes a change in the pressure loading of the latter if the horizontal panel is at a height where the vertical panel has an appreciable gradient, i.e. at a relatively high or low position. Test data substantiate the greater effectiveness of horizontal panels in these positions and the relative ineffectiveness of horizontal panel at the midspan position on the vertical panel (cruciform empennage configuration). At subsonic speeds the vehicle body and horizontal tail affect the flow on the vertical tail in such a way as to increase the effectiveness of the vertical tail. This phenomenon, known as the *end-plate effect*, is represented by an effective change in panel aspect ratio required to give the same lift effectiveness as the actual panel in the presence of the other vehicle components (Ref. [3]).

c. Effect of the wing

For a wing-body combination there are two contributions to the sidewash present at a vertical tail: that due to the body and that due to the wing.

The sidewash due to the fuselage arises from the side force developed on the fuselage at some angle of sideslip. As a result of this side force, a vortex system is produced, which in turn induces lateral-velocity components at the vertical tail. This effect, analogous to the downwash in the longitudinal plane, indirectly affects the incidence of the vertical tail because of the generation of the vortex system. This sidewash from the body causes a destabilizing flow in the airstream beside the body. Above and below the fuselage, however, the flow is stabilizing.

The sidewash arising from a wing in yaw is small compared to that of a body. The flow above the wake centerline moves inboard and the flow below the wake centerline moves outboard.

For conventional aircraft the combination of the wing-body flow fields is such as to cause almost no sidewash effect below the wake centreline (Ref. [3]).

At this point, it is possible therefore to understand the aim of this thesis. The purpose of this work is the experimental investigation of a modular aircraft model in the wind

tunnel of our department to provide data about aerodynamics interference among aircraft components in sideslip condition.

The model's geometry is representative of a typical regional turboprop transport aircraft as those shown in figure 1.4 and table 1.1. A bigger emphasis has been given to the vertical tail plane and to the fuselage since these are the most important components in aircraft directional stability.

It should be noted that this thesis is only a small part in a larger research work, carried out by researchers of our department, in order to validate a new method to predict aircraft static directional stability (details in Ref. [4]).

Tab. 1. 1 – Large turboprop aircraft main characteristics

	ATR-72	Dash8-Q400
Crew	2+2	2+2
Passengers	70	78
Takeoff mass, kg	23 000	27 995
Empty mass, kg	12 850	17 148
Fuselage length, m	27.17	32.81
Fuselage slenderness ratio	10.10	12.20
<i>Wing</i>		
Planform area, m ²	61.00	63.08
Span, m	27.05	28.42
Aspect ratio	12.0	12.1
Root airfoil thickness	18 %	18 %
Tip airfoil thickness	13 %	12 %
<i>Horizontal tail</i>		
Planform area, m ²	12.00	14.56
Span, m	8.10	7.85
Aspect ratio	4.4	4.3
Tail-to-wing area ratio	0.20	0.23
Tail volume coefficient	1.13	1.96
<i>Vertical tail</i>		
Planform area, m ²	12.00	14.13
Span, m	4.34	4.28
Aspect ratio	1.57	1.30
Tail-to-wing area ratio	0.20	0.22
Tail volume coefficient	0.10	0.13
<i>Performance</i>		
Cruise speed, km/h	511	648
Service ceiling, m	7620	6250
Range, km	2666	2400
Rate of climb, m/s	9.38	—
Take-off distance, m	1223	1350



(A) ATR-72. Adrian Pingstone / Wikimedia Commons / Public Domain.



(B) Bombardier Dash 8 Q-400. Pedro Aragão / Wikimedia Commons / CC-BY-SA 3.0.

Fig 1. 5 – Typical regional turboprop aircraft

1.2 ADVANTAGES OF A MODULAR MODEL

As will be better explained in chapter 2, the modular aircraft model that has been tested in the wind tunnel of our department has the following features (schematically summarized in Fig 1.6) :

- the wing is straight and untapered with a fixed aspect ratio and with the possibility to provide 3 positions on the fuselage (low, middle, high);
- the fuselage is a narrow body with a circular section and with three different tail cones differentiated by the parameter (z_{ftc}/r_f) ;
- three vertical tail planes with the same sweep angle but different aspect ratio ($AR_v=1$, $AR_v=1.5$ and $AR_v=2$) have been considered;
- the horizontal stabilizer is straight and untapered with a fixed aspect ratio and several possible positions.

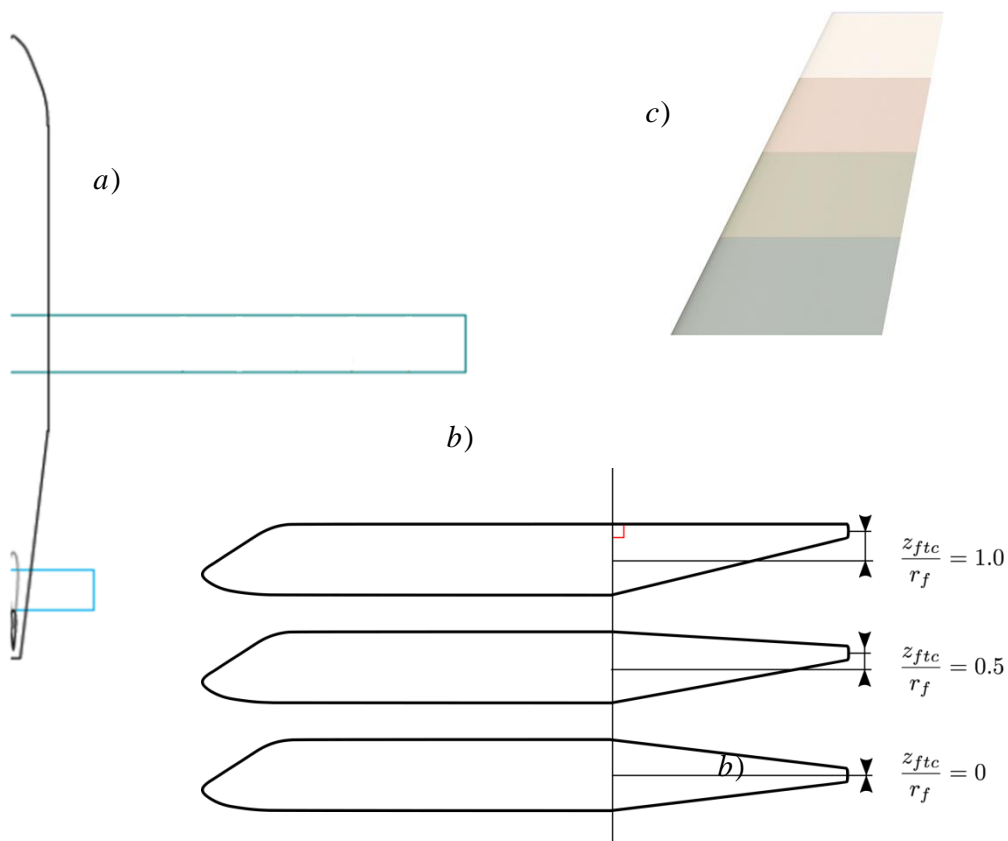


Fig 1. 6 – Layout of configurations investigated

The range of the geometric parameters investigated includes the typical regional turbopropeller airplane layout.

A modular aircraft model, such as the one object of our study, ensures various advantages among which the most important are the following:

- I. possibility to consider partial aircraft configurations, for example body-vertical (BV), wing-body (WB), wing-body-vertical (WBV);
- II. several wing positions, vertical tail plane aspect ratios, horizontal tail plane positions and three fuselages can be arranged in many different combinations (Fig 1.6) in order to investigate many configurations of the typical regional turboprop transport aircraft with a small number of interchangeable components;
- III. possibility to exploit the multiple possible combinations to eventually develop a parametric analysis (Fig 1.7).

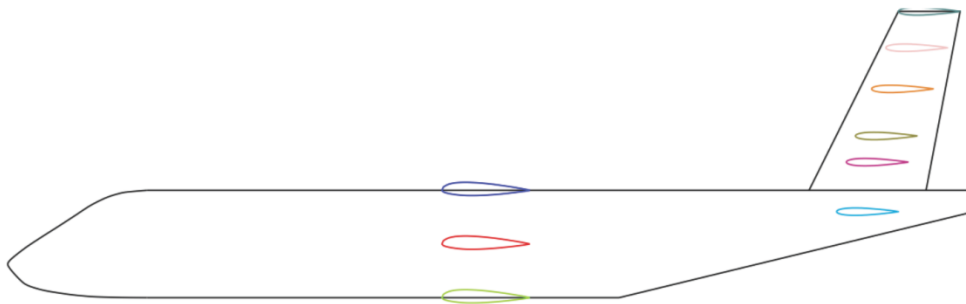


Fig 1. 7 – Some configurations

It should be noted that the geometries of the various components have been kept simple in order to maintain a fair compromise between ease of fabrication of the model and acceptable costs.

1.3 THE PROBLEM OF THE MINIMUM CONTROL SPEED

As highlighted by aeronautic engineering textbooks, the vertical tail plane (Fig 1.8) must provide aircraft directional equilibrium, stability and control in all flight conditions. Landing in a strong crosswind or take-off with one engine inoperative (OEI) are critical conditions defined by authorities that are usually employed in the preliminary sizing of the vertical tail plane, in which the aerodynamic interference of other aircraft components (wing, fuselage, and horizontal tail plane) must be accounted, otherwise it could lead to a heavier and more costly component (if oversized) or to insufficient directional stability (if undersized).



Fig 1. 8 – Example of aircraft vertical tail

For multiengine airplanes the critical design condition for the rudder is nearly always the low-speed flight condition with full asymmetric power. In fact, the failure of one engine at low air speed will create a heavy yawing moment that must be overcome by the rudder in order to maintain flight at zero sideslip (Ref. [1]).

About that, *Minimum control speed* V_{MC} is the calibrated airspeed, at which, when the critical engine is suddenly made inoperative, it is possible to maintain control of the airplane with that engine still inoperative, and maintain straight flight with an angle of bank of not more than 5° .

The airborne minimum control speed may not exceed 1.13 times the reference stall speed hence *it affects the take-off field length*, which must be kept as low as possible, otherwise payload could be reduced on short runways. Here it is sufficient to say that, in OEI condition, the vertical tail has to counteract the airplane asymmetrical thrust. Forces and moments acting on the airplane in OEI conditions are shown in Fig 1.9.

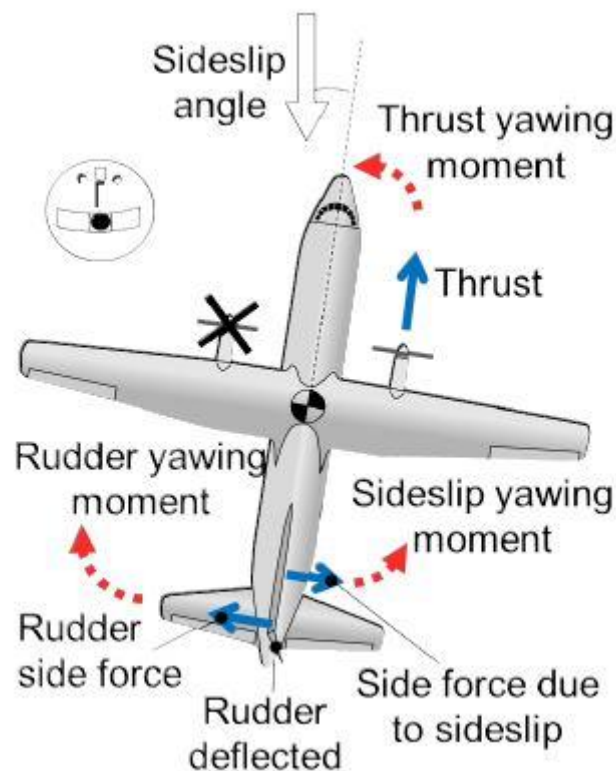
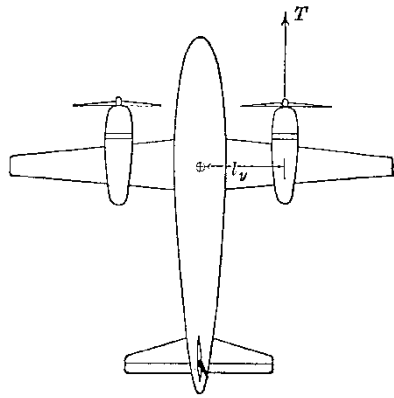


Fig 1. 9 – Most important forces and moments acting on the airplane while using the rudder to counteract the asymmetric thrust and while keeping the wing level.

The propeller-driven engine generates a thrust which decreases with airspeed and the yawing moment due to the asymmetric thrust can be given as follows (Ref [1]), signs are omitted:



$$(1.2) \quad T = \left(\frac{\Pi_a \cdot \eta_p}{V} \right)$$

$$(1.3) \quad N_T = T \cdot l_y = \left(\frac{\Pi_a \cdot \eta_p}{V} \right) \cdot l_y$$

Fig 1. 10 – Yaw moment due to asymmetric power

The rudder at full throw gives a yawing moment (signs are omitted):

$$(1.4) \quad N_v = \frac{1}{2} \rho V^2 \cdot S \cdot b \cdot C_{N\delta_r} \cdot \delta_r$$

$$(1.5) \quad C_{N\delta_r} = C_{L\alpha_v} \cdot \tau_r \cdot \frac{S_v}{S} \cdot \frac{l_v}{b} \cdot \eta_v$$

where

$C_{N\delta_r}$ is the rudder control power

$C_{L\alpha_v}$ is the lift curve slope of the vertical tail;

$\tau_r = \left(\frac{\partial \beta}{\partial \delta_r} \right)$ is the rudder effectiveness; η_v is the dynamic pressure ratio

$\left(\frac{S_v}{S} \cdot \frac{l_v}{b} \right)$ is the vertical tail volume coefficient;

Basically, semi-empirical methods provide a way to calculate aircraft directional stability and control by including the effects of the wing, fuselage and horizontal tail in the $C_{L\alpha_v}$ term. The rudder control may be approximated as:

$$(1.6) \quad C_{N\delta_r} = C_{N\beta_v} \cdot \tau_r$$

where the static stability derivative $C_{N\beta_v}$ includes the above-mentioned effects. Thus, the calculation of directional control authority can be calculated, at least in a first approximation, from the directional static stability derivative. It is important to note that equation 1.6 is an approximation because the effects of aerodynamic interference are not the same of the static stability case.

However, once it has been estimated $C_{N\beta_v}$, the intersection of the two curves $N_T = f(V/V_{sTO})$ and $N_v = f(V/V_{sTO})$ can be used to a preliminary vertical tail surface sizing, according to airborne minimum control speed.

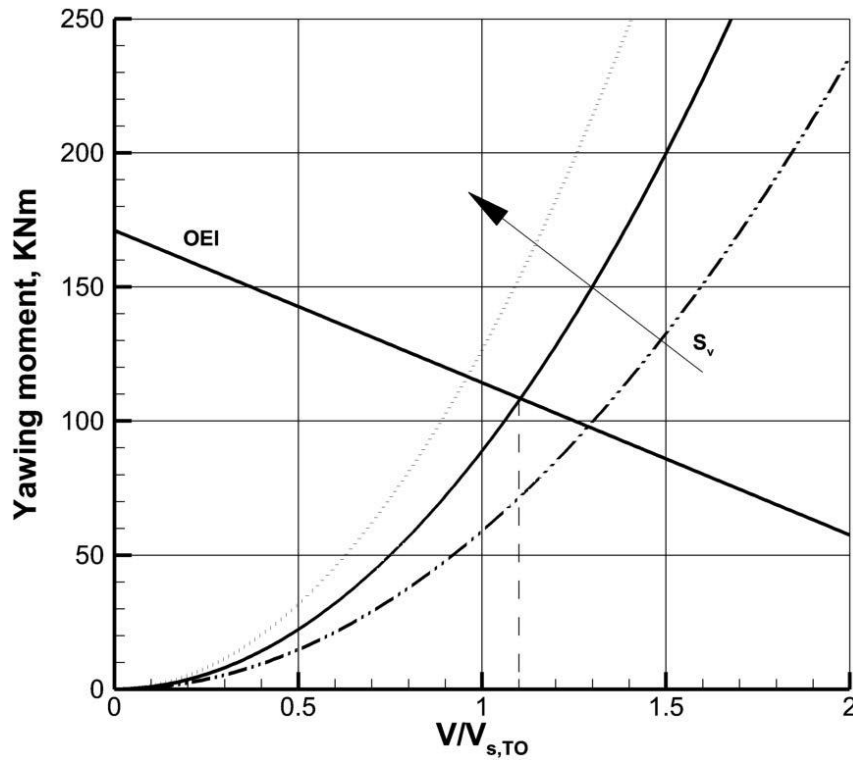


Fig 1. 11 - Chart to preliminary select the vertical tail area S_v according to airborne minimum control speed limit

CHAPTER 2 - THE EXPERIMENTAL MODULAR MODEL

2.1 INTRODUCTION TO THE MODEL

As mentioned in Chapter 1, the purpose of this thesis is the experimental investigation of a modular aircraft model in the wind tunnel of our department to provide data about aerodynamics interference among aircraft components in sideslip condition.

The aircraft model for the wind tunnel has been designed to have interchangeable components, since the objective of the experimental investigations is to provide aerodynamic data (force and moment coefficients) for many configurations. The modular model has also been designed easy to setup quickly in order to switch among configurations in a short time.

The experimental model is made from the following main components which details will be described in the following sections of this chapter:

1 fuselage nose;

1 fuselage cabin;

3 fuselage tail-cones;

1 wing;

2 horizontal tail planes (2 semi-span pairs);

3 vertical tail planes ($AR_V = 1$; $AR_V = 1.5$; $AR_V = 2$).

The model main dimensions are reported in Fig 2.1. It is 2.0 m long and 1.5 m wide. The wing span is limited by the wind tunnel test section width. The aspect ratio is held to $AR = 8.27$. The model total height (with $AR_V = 2.0$ vertical tail) is about 0.6 m. The complete model weighs up to 40 kg, with a center of gravity close to the wing leading edge. The CAD model has been realized in SOLIDWORKS® by

researchers of our department. The complete list of the components is reported in Fig 2.2 and Tab 2.1.

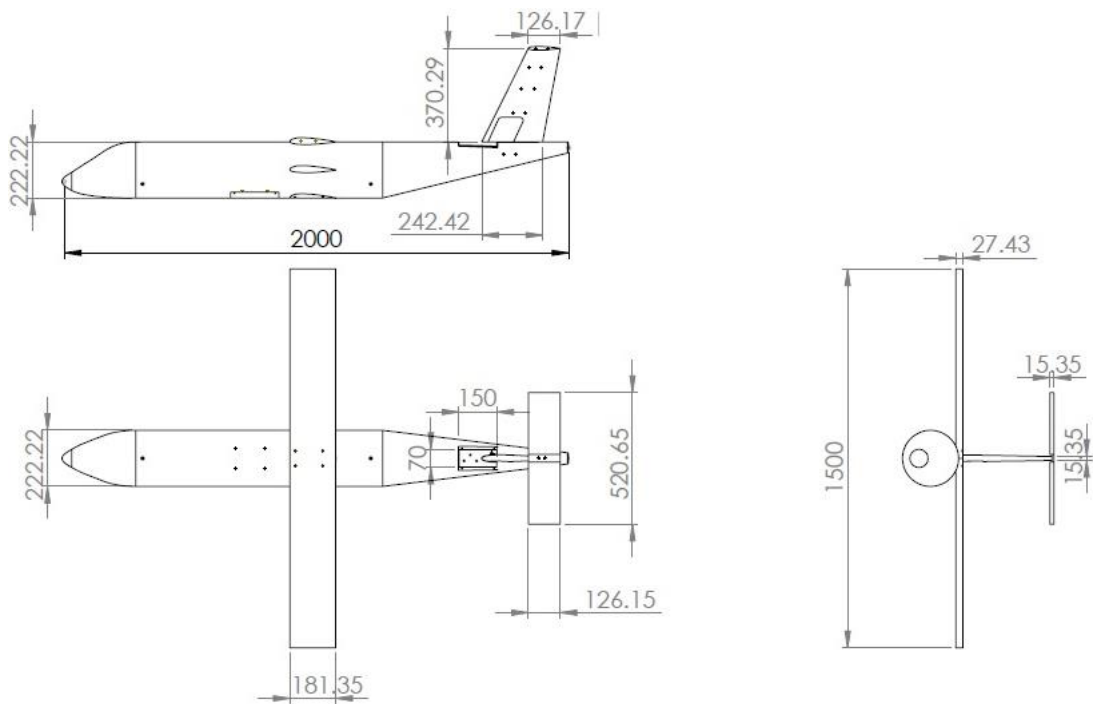


Fig 2. 1 – Model main dimensions (units in mm)

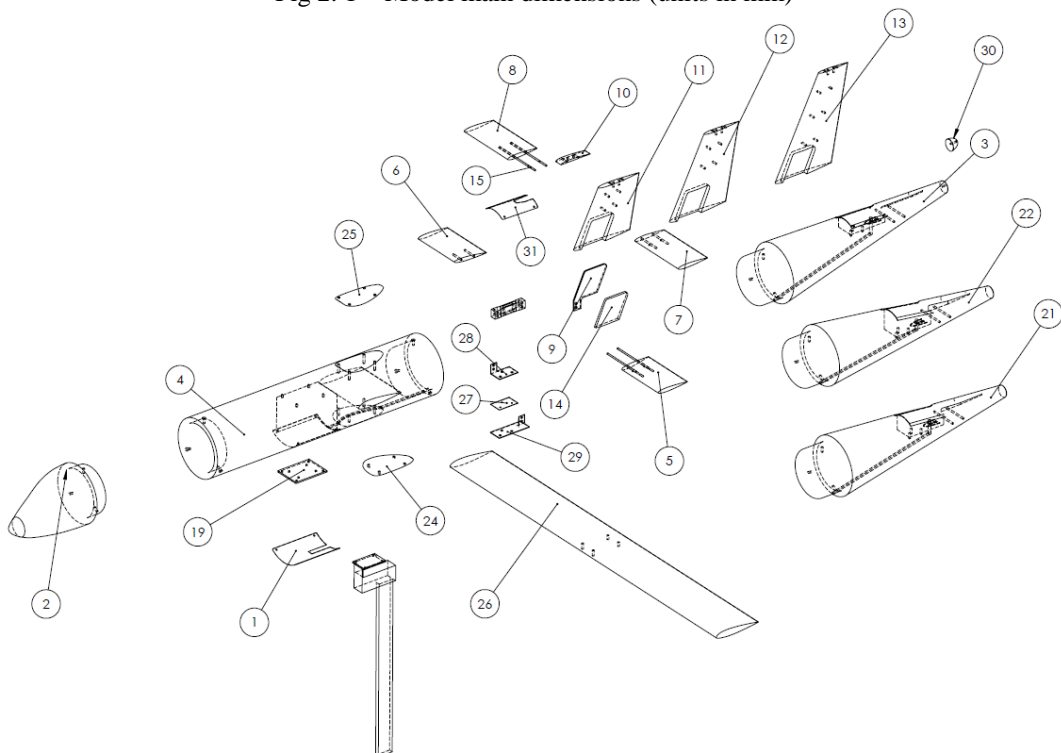


Fig 2. 2 – Model exploded view. The markings correspond to the items of Tab 2.1

Tab. 2. 1 – Bill of materials. Surface and volume are reported only for the machined components. Items are shown in Figure 2.2

Item	Description	Q.ty	Surface (cm ²)	Volume (cm ³)
1	Sheet covering wind tunnel balance	1	n.a.	n.a.
2	Fuselage nose	1	2201.66	7789.57
3	Fuselage tail-cone $z_{ftc}/r_f = 1$	1	4343.85	13 730.58
4	Fuselage cabin	1	10 142.43	29 703.78
5	Left horizontal tail (fuselage)	1	592.19	280.54
6	Right horizontal tail (fuselage)	1	591.63	280.66
7	Left horizontal tail (T empennage)	1	690.67	325.44
8	Right horizontal tail (T empennage)	1	690.01	325.60
9	Vertical tail web	3	n.a.	n.a.
10	T empennage cover	1	92.88	19.14
11	Vertical tail $A_v = 1.0$	1	1019.83	606.92
12	Vertical tail $A_v = 1.5$	1	1296.00	796.99
13	Vertical tail $A_v = 1.0$	1	1508.75	916.57
14	Vertical tail cover	3	225.51	91.37
15	Horizontal tail spar (bar)	4	n.a.	n.a.
19	Interface plate wind tunnel balance	1	n.a.	n.a.
20	Wind tunnel balance	1	n.a.	n.a.
21	Fuselage tail-cone $z_{ftc}/r_f = 0$	1	4396.79	13 528.05
22	Fuselage tail-cone $z_{ftc}/r_f = 0.5$	1	4468.52	13 316.18
24	Wing-fuselage cover (bottom)	1	357.16	142.87
25	Wing-fuselage cover (top)	1	287.28	77.55
26	Wing	1	5691.37	5105.80
27	Trimming support plate	1	n.a.	n.a.
28	Vertical tail load cell support plate	1	n.a.	n.a.
29	Vertical tail support plate	1	n.a.	n.a.
30	Stern fillet	1	59.65	25.93
31	Sheet covering fuselage tail-cone	1	n.a.	n.a.

The CAD model has subsequently been mainly realized by computer numerical control (CNC) milling. The company that has been chosen for the manufacturing is NAET Srl (www.naetsrl.it) located in Villa Literno (CE), Italy. The non-metal parts are made from a high density machinable polyurethane slab named PROLAB 65 (Tab 2.2).

Property	Unit	Value
Color	n.a.	brown
Density at 23 °C	g/cm ³	0.65
Hardness	Shore D1	63
Flexural modulus	MPa	1000
Flexural strength	MPa	34
Compressive strength	MPa	28

Tab. 2. 2 – Prolab 65 properties.

It has the following characteristics (as reported in the specification sheet):

- non-porous material;
- excellent surface aspect (direct paint after sanding);
- very good dimensional stability;
- machining by hand or by machine with wood cutting tools or aluminum cutting tools.

All the manufactured components are shown in Fig 2.3 and Fig 2.4 (metals parts).



Fig 2. 3 – Sanded parts



Fig 2. 4 – Metals parts



Fig 2. 5 - Wing

2.2 WING

The wing is shown in Figure 2.5. It has a straight untapered planform with an airfoil section NACA 23015, typical for regional turbopropeller transport airplane. The main wing's characteristics are summarized in table 2.3. Four countersunk M6 screws are used to attach the wing in high and low wing positions in fuselage.

<i>Wing's characteristics</i>	<i>Unit</i>	<i>Value</i>
Span	m	1.5
Reference area	m ²	0.27
Aspect ratio		8.27
Chord	mm	181.18
Dihedral angle	deg	0
Alpha zero lift	deg	-1.5
$C_{L\alpha}$	1/deg	0.078

Tab. 2. 3 - Wing's characteristics

2.3 FUSELAGE NOSE

The fuselage is a narrow body with a circular section and it is formed by three components: fuselage nose, fuselage cabin and fuselage tail-cone. It is 2.0 m long and the dimensions of every component of the fuselage are shown in Tab 2.4.

Description	Length (m)	Width (m)
Fuselage nose	0.293	0.222
Fuselage tail-cone	0.733	0.222
Fuselage cabin	0.978	0.222

Tab. 2. 4 – Dimensions of the fuselage components

The fuselage nose is the component shown in Fig 2.6 (a) and (b). The first is the CAD image of the nose which reports the main dimensions of the nose itself whereas the second reports the manufactured component. The cylinder extruded from its rear is needed to attach the fuselage nose to the cabin and fix their relative positions by three countersunk M6 screws. To provide assembly tolerance when coupling nose and cabin, the extruded cylinder has a diameter of 0.6 mm smaller than its hollow counterpart of the cabin.

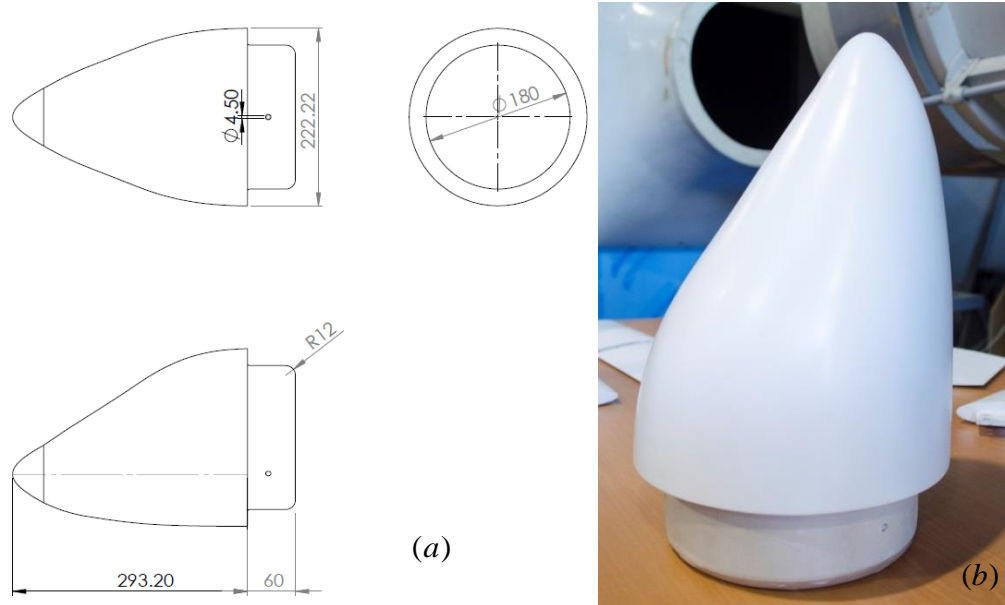


Fig 2. 6 – Fuselage nose: (a) CAD image; (b) manufactured component

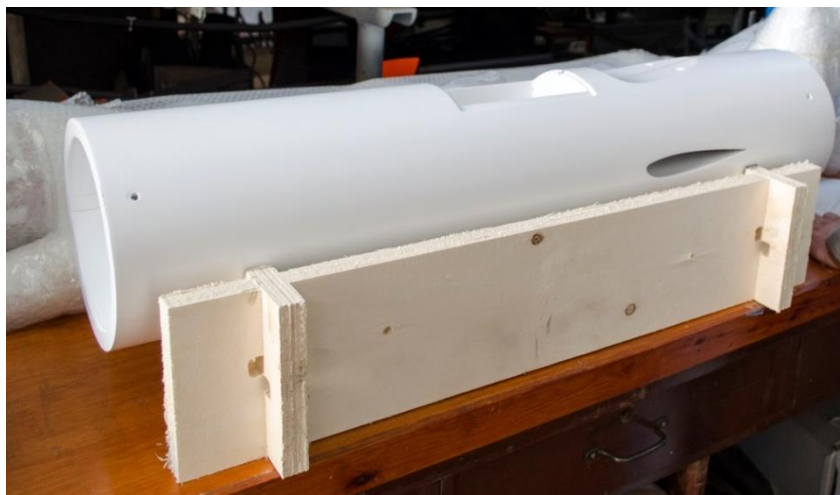


Fig 2. 7 – Fuselage cabin

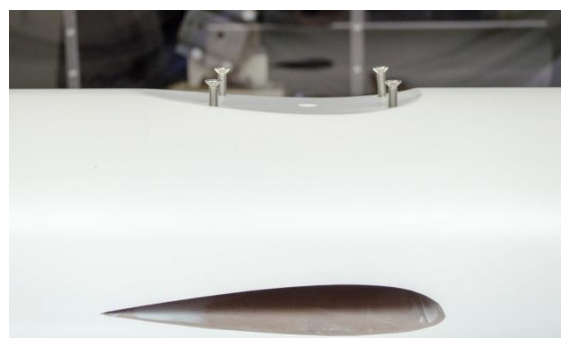


Fig 2. 8 – Two covers Fig 2. 9 – Countersunk to keep wing in high/low position

2.4 FUSELAGE CABIN

The fuselage cabin (Fig 2.7) is the central component to which all the other main parts are linked. It is substantially a cylinder 0.733 m long with a diameter of 0.222 m as shown in Tab 2.4.

It provides housing for the wind tunnel balance, obtained by hollowing the central, lower part. It allows the wing to be placed in low, mid, and high position. Four countersunk M6 screws have been provided to keep the wing in high and low wing positions (see Fig 2.9), whereas to prevent the wing to slide from the mid position, a pin may be inserted through the fuselage from above.

Under the wing position, the continuity of the fuselage cabin's surface is ensured by means of two covers. These little components are shown in Fig 2.8 and are marked as 24 and 25 in Tab 2.1.

2.5 VERTICAL TAIL

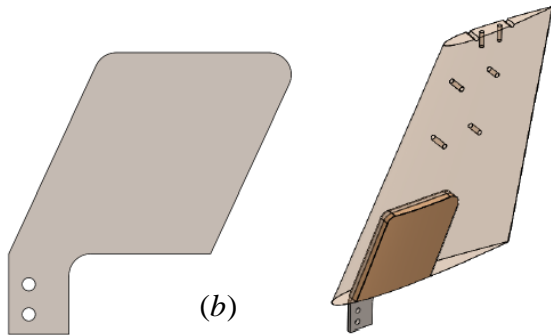
Three vertical tails, shown in Fig 2.10 (a), are used for the experimental investigation of the model in the wind tunnel of our department. They have the same planform and the same leading edge sweep angle $\Lambda_{LE} = 26.6^\circ$. The airfoil section is a NACA 0012. Their main characteristics, together with those of all lifting surfaces of the model, are summarized in the Tab 2.5.

ID	Description	AR	λ	S (m ²)	c_{root} (m)	c_{tip} (m)	b (m)
26	Wing	8.27	1.0	0.273	0.182	0.182	1.5
5 to 8	Horizontal tail	4.1	1.0	0.055	0.128	0.128	0.521
11	Vertical tail	1.0	0.73	0.036	0.242	0.177	0.210
12	Vertical tail	1.5	0.62	0.048	0.242	0.151	0.295
13	Vertical tail	2.0	0.53	0.057	0.242	0.128	0.370

Tab. 2.5 – Dimensions of the lifting surface of the model.
(Items ID are shown in Fig 2.2)

As can be seen from the above table, the root section chord is the same for the three planforms, the taper ratio λ varies from 0.53 to 0.73, and the aspect ratios AR_V investigated are 1.0, 1.5, and 2.0.

As it can be seen from Fig 2.10 (a), each planform presents pairs of holes at several span stations. These are used to insert horizontal tail spars to get different empennage configurations.



The vertical tail is linked to the fuselage by a plate, acting as a structural web and shown virtually in Fig 2.10 (b), which is sunk in the former.

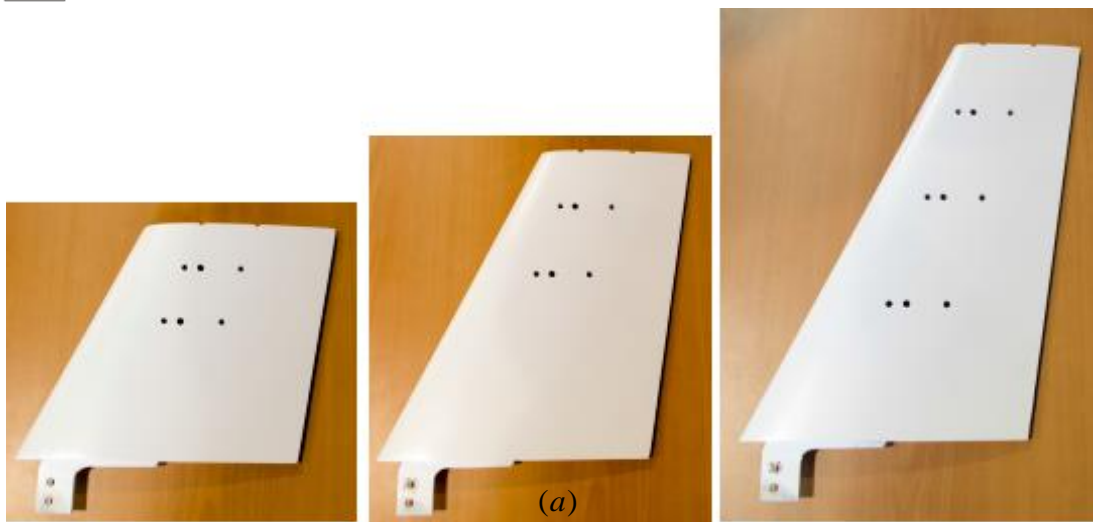


Fig 2. 10 - (a) Vertical tails comparison ($AR_v=1 - 1.5 - 2$); (b) Vertical plate.



Fig 2. 11 – (a) Fuselage tail cones; (b) Sterns of the tail cones

2.6 FUSELAGE TAIL-CONE

Three different fuselage tail cones, shown in Figure 2.11, are provided to investigate the effects of the wing-body wake on the empennage. Each tail cone is 0.733 m long (see Tab 2.4) but have a different value of the parameter (z_{fic}/r_f) , where r_f is the radius of the fuselage cabin, while the meaning of z_{fic} is clear by looking at Fig 2.12. The tail cone is a crucial component, because it must:

- support the empennage
- be stiff enough to not be deformed under aerodynamic loads
- be easily handled during the change of configuration
- not weigh too much on the fuselage cabin

In order to get experimental data about the vertical tail in various aircraft configurations, a solution allowing the direct measure of the aerodynamic force on the empennage has been designed.

More in detail, the vertical stabilizer must be attached to a separate load cell, which, in turn, is attached to the fuselage. For this purpose each tail cone is provided of an appropriate space to allow load cell and empennage mounting (see Fig 2.13). It provides enough volume to protect the load cell and supporting plates from the aerodynamic flow. Moreover, there is a duct to allow the take out the data acquisition cable through a slot on the bottom fuselage surface. The slot continues on the fuselage cabin allowing the cable to be taken to the wind tunnel balance sting, thus avoiding aerodynamics interference, and then to the acquisition system.

As shown in Fig 2.13, the only constraint between the vertical tail and the fuselage is the load cell (that will be described in Chap 3), which is linked to the fuselage on one side and to the vertical stabilizer on the other side. Thus, the latter is suspended on the load cell, since no contact can be allowed with the fuselage to avoid the direct transmission of the aerodynamic loads from the tail to the body, in order to measure the aerodynamic forces acting on the vertical tail in a given aircraft configuration. For this reason, an empty space few millimetres thick between the vertical tail root section and the fuselage has been provided.

The empennage assembly, the load cell and a description of the load path are reported in Fig 2.14. The idea is to get aerodynamic data from both the vertical tail (through the load cell) and the entire aircraft (through the wind tunnel balance) at the same time, to evaluate the aerodynamic interference following.

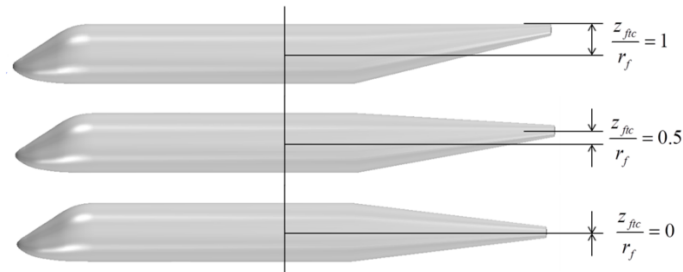


Fig 2. 12 - $\left(\frac{z_{fbc}}{r_f}\right)$ parameter



Fig 2. 13 – Vertical tail assembly with load cell

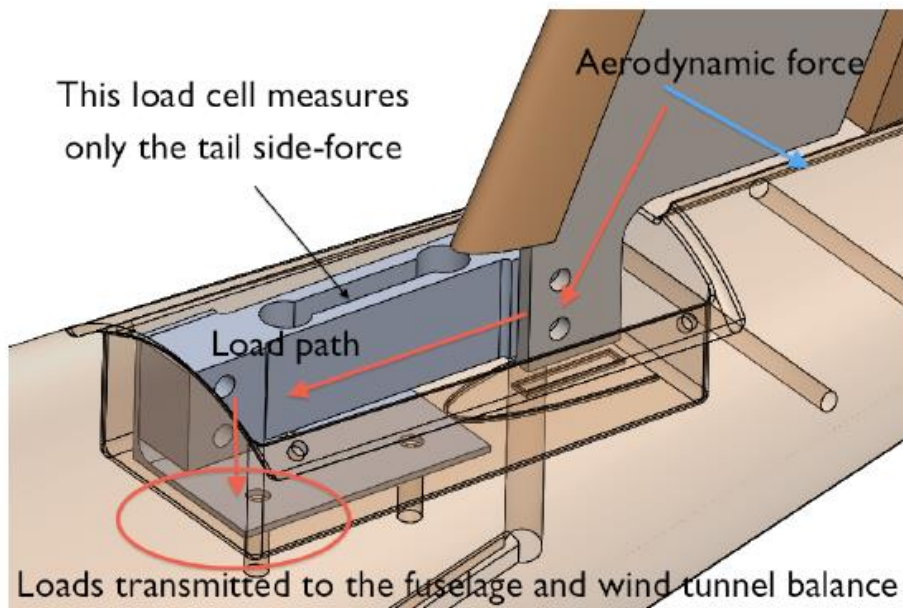


Fig 2. 14 – Loads path with the vertical tail load cell

2.7 HORIZONTAL TAIL

As already mentioned in section 2.1, there are two pairs of horizontal tail semi-span, shown in the following figures:

- one for the body-mounted tail configuration, see Fig. 2.15 (A);
- the other for the tail-mounted configuration, see Fig 2.15 (B).

Both have a NACA 0012 as airfoil section but the former has been cut such to be fit on the fuselage tail-cone.

The two horizontal tails are straight and untapered with a fixed aspect ratio $AR_H = 4.1$. Both have a chord 0.128 m long, a surface of 0.055 m² and a span of 0.521 m.

As it can be seen from Fig 2.15 (A) and (B), the tail spars are two aluminium bars that are fixed to one side and locked each other on the other side by two M2 screw.

2.8 OTHER SMALL COMPONENTS

There are other small components that are not described in the previous sections:

- the wind tunnel balance and the tail load cell are covered by folded metal sheets, shown Fig 2.16;
- the tail-cone stern can be filleted by adding the components shown in the Fig 2.18;
- between the model and the lateral-directional wind tunnel balance there is an iron interface plate shown in Fig 2.17;
- the T-tail configuration presents an additional element, which must be attached on the vertical tail tip to provide a constraint for the horizontal stabilizer.

Fig 2. 15 – Horizontal tail: (A) Body mounted; (B) Tail mounted



Fig 2. 16 – Covers aluminium sheets

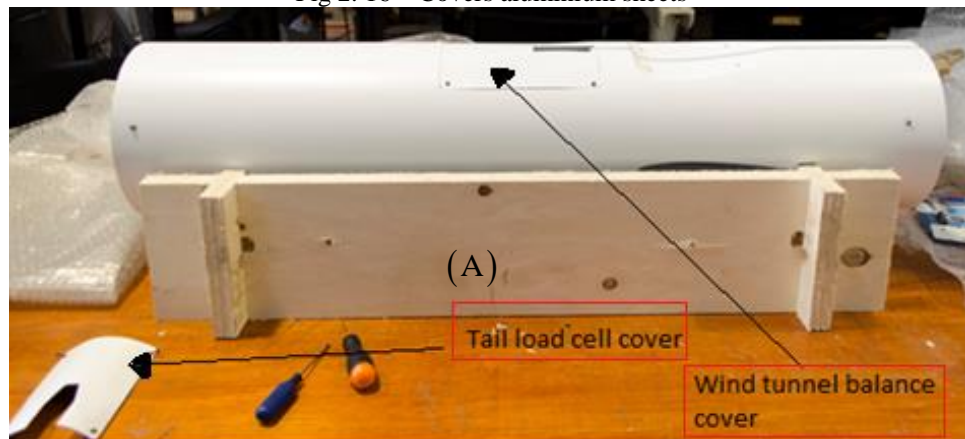


Fig 2. 17 – Iron interface plate

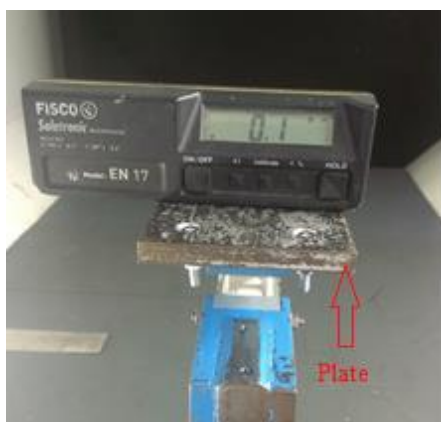


Fig 2. 18 – Tail-cone stern fillet

CHAPTER 3 - APPROACH TO WIND TUNNEL TESTING

3.1 INTRODUCTION

Wind tunnels offers a rapid, economical, and accurate means for aerodynamic research, because they make it possible to use models and because they are always available.

The earliest wind tunnels were invented towards the end of the 19th century, in the early days of aeronautic research. The wind tunnel was envisioned as a means of reversing the usual paradigm: instead of the air standing still and an object moving at speed through it, the same effect would be obtained if the object stood still and the air moved at speed past it. Benjamin Robins (1707-1751), an English military engineer and mathematician, invented a whirling arm apparatus to determine drag and did some of the first experiments in aviation theory. Sir George Cayley (1773-1857) also used a whirling arm to measure the drag and lift of various airfoils. However, at the end of the 19th century, the major fault of the whirling arm was apparent. This fault was due that the wing was forced to fly in its own wake. Francis Herbert Wenham (1824-1908), a Council Member of the Aeronautical Society of Great Britain, addressed these issues by inventing, designing and operating the first enclosed wind tunnel in 1871. Konstantin Tsiolkovsky built an open-section wind tunnel with a centrifugal blower in 1897, and determined the drag coefficients of flat plates, cylinders and spheres. In the early 1890s a Danish inventor, Poul la Cour, applied wind tunnels in his process of developing and the technology of wind turbines. Carl Rickard Nyberg used a wind tunnel when designing his Flugan from 1897 and onwards. In a classic set of experiments, the Englishman Osborne Reynolds (1842-1912) of the University of Manchester demonstrated that the airflow pattern over a scale model would be the same for the full-scale vehicle if a certain flow parameter were the same in both cases. This factor, now known as the Reynolds number, is a basic parameter in the description of all fluid-flow situations. This comprises the central scientific justification for the use of models in wind tunnels to simulate real-life phenomena. The Wright brothers' use of a simple wind tunnel in

1901 to study the effects of airflow over various shapes while developing their Wright Flyer was in some ways revolutionary. In France, Gustave Eiffel (1832-1923) built his first open-return wind tunnel in 1909, running about 4000 tests between 1909 and 1912 and contributing to set new standards for aeronautical research. Eiffel's contribution into improvement of the open- return wind tunnel by enclosing the test section in a chamber was followed by a number of wind tunnels later built (Eiffel was also the first to design a flared inlet with honeycomb flow straightener). Subsequent use of wind tunnels proliferated as the science of aerodynamics and discipline of aeronautical engineering were established and air travel and power were developed. The US Navy in 1916 built one of the largest wind tunnels in the world at that time at the Washington Navy Yard. Until World War Two, the world's largest wind tunnel was built in 1932-1934 and located in a suburb of Paris, Chalais-Meudon, France. It was designed to test full size aircraft and had six large fans driven by high powered electric motors. The Chalais Meudon wind tunnel was used by ONERA under the name S1Ch until 1976, e.g. in the development of the Caravelle and Concorde airplanes. Today, this wind tunnel is preserved as a national monument. During the Second World War large wind tunnels were built, and the development of wind tunnel science accompanied the development of the flying machines. In 1941 the US constructed one of the largest wind tunnels at that time at Wright Field in Dayton, Ohio. The wind tunnel used by German scientists at Peenemünde prior to and during WWII is an interesting example of the difficulties associated with extending the useful range of large wind tunnels. By the end of World War Two, the US had built eight new wind tunnels, including the largest one in the world at Moffett Field near Sunnyvale, California, and a vertical wind tunnel at Wright Field. Later on, wind tunnel study came into its own: the effects of wind on man-made structures or objects needed to be studied when buildings became tall enough to present large surfaces to the wind, and the resulting forces had to be resisted by the building's internal structure. Determining such forces was required before building codes could specify the required strength of such buildings and such tests continue to be used for large or unusual buildings. Still later, wind-tunnel testing was applied to automobiles, not so much to determine aerodynamic forces per

se but more to determine ways to reduce the power required to move the vehicle on roadways at a given speed (Ref. [5]).

3.2 WIND TUNNEL OF THE DII

The experimental tests campaign has been performed in the main subsonic wind tunnel facility of the DII (*Department of Industrial Engineering*).

This is a subsonic, closed circuit tunnel, with a tempered rectangular cross section as shown in Fig 3.1 and Fig 3.2. Main test section has a 4 meters length with a maximum achievable speed of 50 m/s and low turbulence level equal to 0.1%. The main wind-tunnel characteristics are summarized in Tab 3.1.



Fig 3. 1 - Main subsonic wind tunnel facility

Test section dimensions	2.0 m × 1.4 m
Maximum available wind speed	50 m/s
Turbulence level	0.10 %
Maximum power	150 kW

Tab 3. 1 – Wind tunnel of the DII, main characteristics

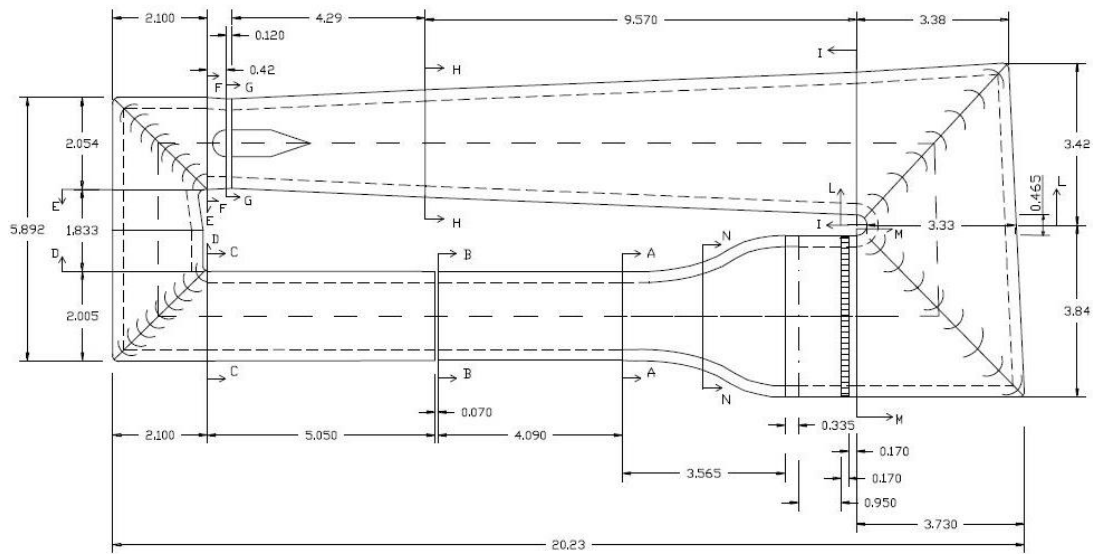


Fig 3. 2 - Plane form and geometric dimensions of the DII's wind tunnel facility

The main components of the closed circuit tunnel are shown in the Fig 3.2 and are described in the following. Capitals letters refer to the sections of Fig 3.2.

- **Test section:** it is 4 m long, 2 m wide and 1.4 m high. Its cross section is rectangular, with blunted edges and with an area of 2.68 m^2 . Sections from A to B;
- **Diffusers:** there are three diffusers in order to slow down the airflow coming from the test chamber. The first diffuser (B-C) has a length of about 5 m and an expansion angle of about 3° and it links the last section of the test chamber to first corner. The second diffuser (D-E) is placed between the first two corners and has a length of about 1.8 m. The last diffuser (G-I) is the longest one (about 12.3 m) and increases the tunnel section having an expansion angle of about 3° . It is placed between the second and third corner;
- **Screen:** it is placed immediately before the first corner (section C) with the aim to protect the turning vanes against any possible object or scraps that could be lost by the model in the test section. The screen has squared cells of about 13 mm for edge;

- **Corners:** the first corner (C-D) is placed behind the first diffuser and has a constant section with turning vanes with a chord of about 450 mm and a maximum thickness of about 14.4%. The second corner (E-F) is placed behind the fan and is equipped with tabs having a chord of about 490 mm and maximum thickness of about 13.3%. The second corner section is slightly divergent, such as the third and fourth corner. The third corner (L-I) has diverters with a chord of 925 mm and maximum thickness of 17.3%, while the fourth corner (L-M) tabs have a length of 875 mm with a maximum thickness of 18.3%;
- **Fan:** it is placed immediately ahead of the second corner (D-E). Upstream the six blades propeller, a four blade flow straightener ring is placed. The ogive of the fan has a maximum diameter of 700 mm;
- **Stagnation chamber:** it has a length of 0.035 m and it is placed ahead of the nozzle. Section M;
- **Honeycomb flow straighteners:** they are elliptical section cells placed at the beginning of the stagnation chamber. Section M;
- **Mesh screen:** it has the function to reduce the turbulence axial component of the flow in the test section allowing a turbulence level of 0.10%;
- **Nozzle:** it has a length of 3.56 m, with an inlet section of about 12.7 m² and an outlet section of 2.7 m², with a ratio of 4.83. Sections from M to N.

3.3 INSTRUMENTATION

The instrumentation used to perform the experimental test campaign can be divided in: measurement, control, data acquisition and elaboration.

3.3.1 Measurement instrumentation

This instrumentation consists of an internal lateral-directional strain gage balance for the measurement of aerodynamic forces and moments, an off-center load cell in order to have the direct measure of the aerodynamic force acting on the vertical tail, a Venturi system to measure the dynamic pressure, an inclinometer to read the longitudinal attitude of the model, a potentiometer to measure the sideslip angle and finally a temperature probe to measure the static temperature in the test section. Some details are given in the following:

- **Lateral-directional strain gage balance:** the internal balance with three channels shown in Fig. 3.3 has been used for the lateral-directional measurements of side force, yawing and rolling moments. It is made from an Al-2024-T3 aluminum block. The lower part of the fuselage cabin of the model provides a special compartment for housing the balance.

The balance has been subjected to a calibration procedure in order to perform a right estimation of the aerodynamics forces and moments. The calibration has been previously performed by Corcione (Ref [5]), who followed the procedure described in the book of Barlow, Rae, and Pope (Ref [6]). The calibration procedure is also essential to estimate the balance center in order to transfer forces and moments to the desired reference point, e.g. the 25% of wing m.a.c. The actual balance readings have been deeply verified by applying the combination of predicted loads to be encountered during the tests. layout of the test model.

Corrections have been provided to account for the combination of weight, pitching moment, rolling moment, and yawing moment, due to the particular layout of the test model, see Section 3.5.1.

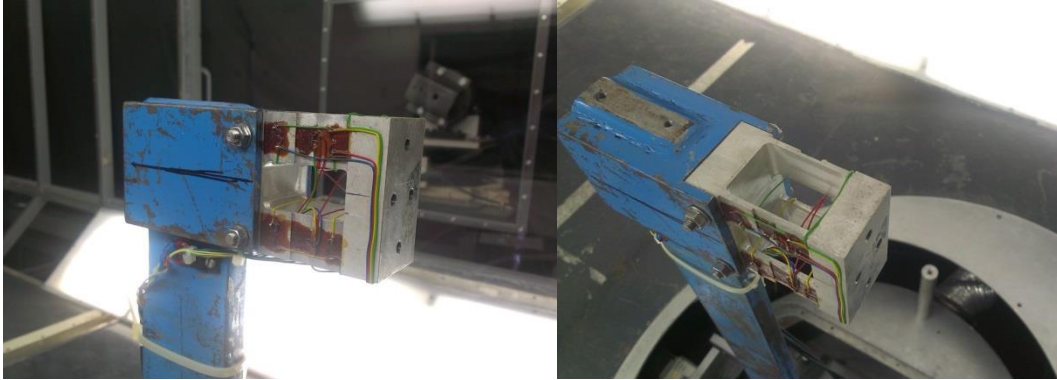


Fig 3. 3 - Lateral directional strain gage balance

- **Off-center load cell:** it is a Picotronic AAC model, used to directly measure the side force generated by the vertical tail. It is made from aluminium alloy and it has 15 Kgf full scale, with $2.0\text{mV/V} \pm 10\%$ nominal sensitivity. Its dimensions are 130 x 30 x 22mm. The load cell can measure forces in the side direction, colored in white in Fig 3.4. Its location on the model has been discussed in the chapter 2 (exactly Section 2.6) and has been shown in Fig 2.13 and Fig 2.14, whereas its calibration are discussed in Section 3.5.1.

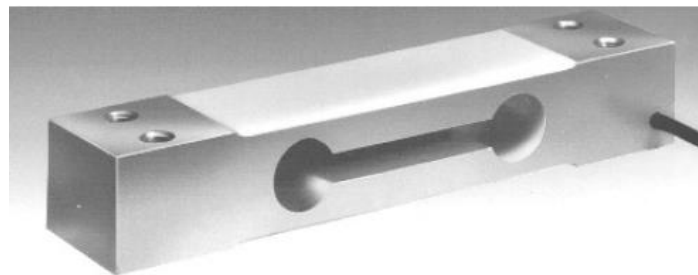


Fig 3. 4 - The off-center load cell



Fig 3. 5 - Inclinometer

- **Venturi:** the wind tunnel of the DII is equipped with 4 static pressure probe placed on both faces of both initial and final sections of the convergent. A pressure transducer (with a F.S. of 2500 Pa and an accuracy of 2-3 Pa) measures the static pressure variation between these sections and through the continuity equation obtains the dynamic pressure at the exit of the nozzle. Several tests without the model in the test section and at different air speeds, have shown that the dynamic pressure at the end of the nozzle is not equal to the test section dynamic pressure, but the linear fit shown in Eq. 3.1 has been found:

$$q_{eff} = 1,09 \cdot q_{means} \quad (3.1)$$

Because it is impossible to use a Pitot probe to measure the dynamic pressure in the test section in presence of the scale model (the test section should be long enough to guarantee that the measure is not affected by the pressure field produced by the model in the test section), the only available measure of the dynamic pressure is obtained by the *Venturi*, thus the above equation is assumed to be valid also in presence of the scale model in the test section.

- **Inclinometer:** it is the uni-axial tilt Sensor CXLA01, produced by CrossBow (San Jose, CA-USA) and shown in Fig 3.5. The sensor measures the component of the acceleration of gravity that lies in the plane of the instrument reference face. The inclinometer has been integral mounted with the sting on which the balance is fixed on.
- **Potentiometer for the sideslip angle:** the sideslip angle has been measured through the use of a potentiometer (shown in Fig 3.6) with an accuracy of 0.1°. Once installed, the available range for the sideslip angle β is from -15° to 25°. The sideslip angle is assumed to be positive in sign when the airflow comes from the left wing the model. This is the opposite of the usual convention because of the operator's point of view of the test chamber.

- **Temperature probe:** it consists of a flush wall-mounted probe for the measurement of the static temperature in order to determine the true test section speed through the use of Bernoulli's incompressible equation and to obtain the mass density through the equation of state. The temperature measurements are also needed to take under control the heating of the strain gage sensors that are affected by temperature change, which during a test ranges from 30° to 50°, depending on the environment temperature too.

3.3.2 Control instrumentation

The control instrumentation used in this test campaign is shown in Fig 3.7. It consists of a kinematic mechanism (manhandle by the operator) with a crank handle fixed at the end of a horizontal shaft acting as worm-screw. This shaft transmits the rotatory motion to the vertical axis of a small diameter gear wheel. The rotatory motion is then transmitted to a larger gear wheel through a steel chain reducing the angular velocity of the model. A steel plate, which is at level with the floor, is fixed to the axis of the second gear wheel. The steel plate allows the whole assembly sting-balance-model to rotate.

3.3.3 Acquisition and elaboration

This instrumentation for acquisition and elaboration consists in:

- a 16 channels device for the acquisition and conversion into 16 bit (SPARTAN system, produced by Imc Data Works) of output data coming from the measurement instrumentation;
- a Desktop PC with Windows XP, provided with an interface software for the A/D converter;
- a software for the elaboration and visualization of the acquired data. The software, named WT6, has been developed at the DII laboratory by ADAG research group.



Fig 3. 6 – Potentiometer



Fig 3. 7 – Sideslip mechanism



Fig 3. 8 – Spartan system 16 channels

3.4 SETUP ISSUES

Before starting the experimental tests campaign two issues had to be solved: model's center of gravity location and stiffening of the sting.

3.4.1 Center of gravity location

For the model investigated, the balance is located in a hollowing forward of the wing. The balance center is obviously the point with respect to which are measured the global aerodynamic forces and moment. This point is located at about 0.71 m, along the longitudinal axis, to the fuselage nose. In the original design configuration the center of gravity of the model was located between the wing aerodynamic center and the leading edge, at about 0.91 m along the longitudinal axis to the fuselage nose. Because the center of gravity of the model does not correspond to the balance center, the original mass distribution produced, in the complete configuration (WBVH, with $AR_V = 2$), a positive pitching moment of about:

$$M_{pitch_w} = W_{initial} \cdot (x_{cg_{initial}} - x_{cb}) \cong 39kg \cdot 0.2 m \cong 8 kg \cdot m \quad (3.2)$$

Since this pitching moment could have penalized the accuracy of the lateral-directional measurements, the location of the model's center of gravity has been suitably modified. To move the center of gravity closer to the balance center, a lead cylinder of about 9.1 Kg was inserted in the fuselage. This balancing mass was internally made to the laboratory of the DII from the fusion of lead pieces of various shapes and it has the following dimensions: diameter $\cong 0.12$ m and height $\cong 0.11$ m.

With the abovementioned process, the weight passed from $W_{initial} \cong 39Kg$ to $W_{final} \cong 48Kg$ but the moment arm of the weight force from the balance center was reduced to $(x_{cg_{final}} - x_{cb}) \cong 0.05 m$. Therefore, the new mass distribution produced a positive pitching moment of about:

$$M_{pitch_w} = W_{final} \cdot (x_{cg_{final}} - x_{cb}) \approx 48kg \cdot 0.05 m = 2.4 kg \cdot m \quad (3.3)$$

This value is much more acceptable than the initial one for the purposes of our measurements. Furthermore, since the wing's profile is not symmetrical and there is an inevitable offset between the lift and the balance center, it will be further reduced by the pitching moment contribution of the wing lift.

Fig 3.9 and Tab 3.2 summarize the situation at different alpha values and $V = 40$ m/s (sea level $\rho = 1.225$ Kg/m³).

In order to make only a preliminary estimation the contribute of the horizontal tail has been neglected. Moreover the horizontal tail's profile is symmetrical and we are interested at the case of not angle of attack.

As we seen from the Tab 3.2, in the worst case, for the model aircraft in its complete configuration at no angle of attack and at wind speed of 40 m/s, the pitching moment respect the balance center is about 1.8 Kgf m.

3.4.2 Stiffening of the sting

The lateral-directional strain gage balance is mounted on a steel sting and the assembly sting-balance is, in turn, linked to a rigid metal support placed below the floor of the test section. The sting was internally made to the laboratory of the DII and it has a rectangular section.

As said in the previous section, the addition of a balancing mass have brought the total weight to about 48 kgf. For this reason, the sting of the balance has been stiffened by soldering an appropriate iron plate on its side (see Fig. 3.10).

This allowed to make much more rigid the assembly sting-balance and reduce unpleasant vibrations that could affect the experimental measures.

The stiffening process described has been realized in the laboratory of the DII under the technical supervision of skilled workers in this field.

Tab 3. 2 - Estimation of pitching moment contributes of weight and lift

WEIGHT (arm from the cb: $\Delta x_{weight}=0.05m$)			WING LIFT (arm from the cb: $\Delta x_{lift}=0.20m$)		
α (deg)	Weight (Kg)	Mom. (Kg m)	α (deg)	Lift (Kg)	Mom. (Kg m)
0	48	+2.4	0	2.9	-0.6
2	48	+2.4	2	6.7	-1.34
5	48	+2.4	5	12.4	-2.48

TOTAL FORCE AND MOMENT (Z-axis positive in the positive lift direction)		
α (deg)	Z-Force (Kg)	Mom. (Kg m)
0	-45.1	+1.80
2	-41.3	+1.06
5	-35.6	-0.08

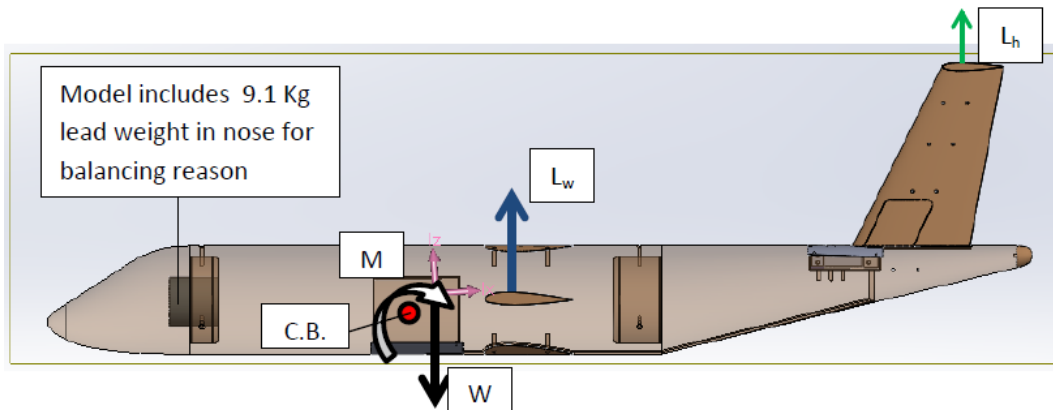


Fig 3. 9 - Model with lead cylinder in the fuselage nose

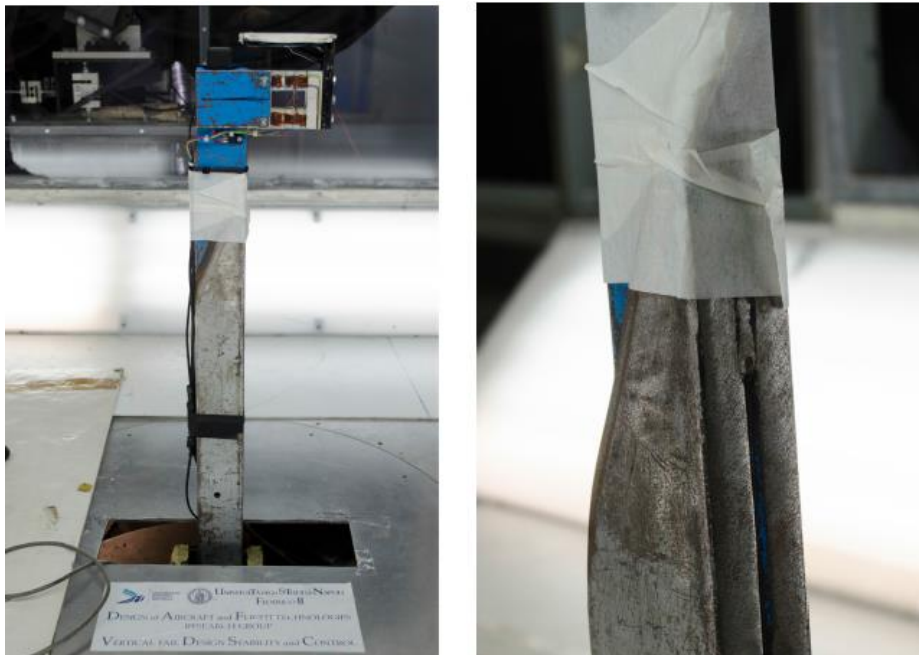


Fig 3. 10 - Sting stiffened

3.5 SETUP OF THE WIND TUNNEL

A preliminary setup of the wind tunnel instrumentation, as well as of the test model, is needed before any operation.

The measurement, control, and elaboration instrumentation must be checked. In particular, the wind-tunnel balance readings must be verified. Then, the model can be mounted in the test section and the whole assembly can be verified in place. Finally, the effects of low Reynolds number can be measured and corrected.

3.5.1 Verification of the balance readings

The internal strain gage balance is a very delicate item. Its readings must be checked prior to every test campaign, since it is the main, if not the unique, source of measurement. This is also essential in order to apply the transportation of forces and moment from the balance center to the desired reference pole for the reduction of the aerodynamic forces and moments.

The verification consists in applying known loads in several positions and acquiring the balance readings. If the acquired data are not consistent with the applied loads, corrections must be provided from the former, e.g. by plotting regression lines that are best fit curves on the charts of gathered data in all load conditions.

The balance readings have been verified in numerous cases, by varying the weight on the balance center, the pitching, yawing, and rolling moments, and the side force applied at several distances from the balance center, in both horizontal and vertical directions. Most of the loads have been applied for the weight and pitching moment conditions discussed in the previous sections.

Results provided that the yawing moment N is not affected by the eccentricity of the applied loads, whereas the sideforce Y and the rolling moment \mathcal{L} do, suggesting the following correction:

$$Y_{corr} = Y_{means} - err_Y(N) - err_Y(\mathcal{L}_{corr}) \quad (3.4)$$

$$\mathcal{L}_{corr} = 0.98[\mathcal{L}_{meas} - err_{\mathcal{L}}(N)] \quad (3.5)$$

Where

Y_{corr} is the sideforce corrected for the effects of yawing and rolling moments

Y_{means} is the uncorrected sideforce read by the wind tunnel software

$err_Y(N)$ is the sideforce error due to the applied yawing moment N

$err_Y(\mathcal{L}_{corr})$ is the sideforce error due to the corrected rolling moment \mathcal{L}_{corr}

\mathcal{L}_{meas} is the measured rolling moment

$err_{\mathcal{L}}(N)$ is the rolling moment error due to the applied yawing moment N

The error functions are defined as

$$err_Y(N) = 0.0034N^3 + 0.0040N^2 - 0.0821N \quad (3.6)$$

$$err_{\mathcal{L}}(N) = 0.0025N^3 + 0.0109N^2 - 0.1118N \quad (3.7)$$

$$err_Y(\mathcal{L}_{corr}) = 0.24\mathcal{L}_{corr} \quad (3.8)$$

which allow the correct results in output.

Finally, the off-center load cell (Section 3.3.1) has been calibrated. The procedure is very simple, since it is a single axis load cell. Its end with the acquisition cable has been fixed to a rigid constraint, with the sensible side parallel to the ground. At the other end a known mass has been suspended. From the tension read on the PC display, the tare constant has been calculated from the simple relationship:

$$Force = K_{cell} \cdot Tension \quad (3.9)$$

where K_{cell} has the dimension of Kgf/V. The tare has then been verified by mounting the cell in the fuselage tail-cone and the vertical tail on the cell and applying a known mass in several positions to check the load cell readings. The installation of the off-center cell has been already described in Section 2.6 and shown in Fig 2.13 and Fig 2.14. Fig 3.11, instead, shows the test of the off-center load cell with the application of a know mass.

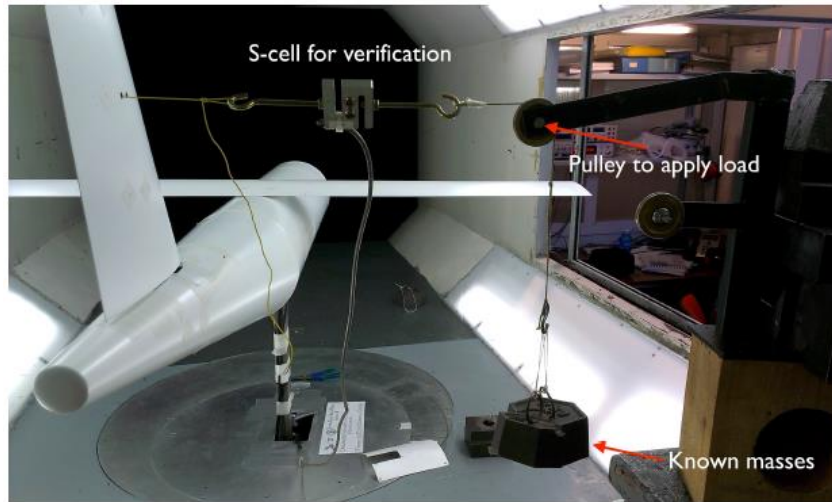


Fig 3. 11 – Test of the off-center load cell

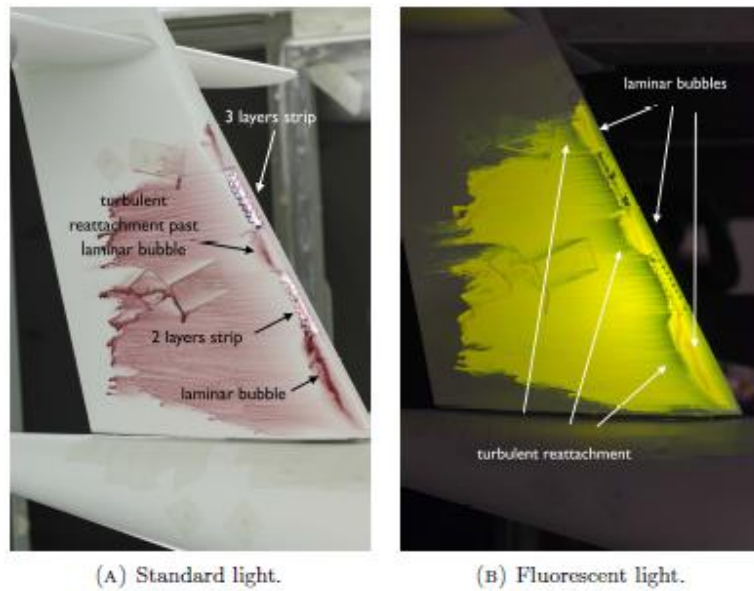


Fig 3. 12 – Flow visualization on vertical tail

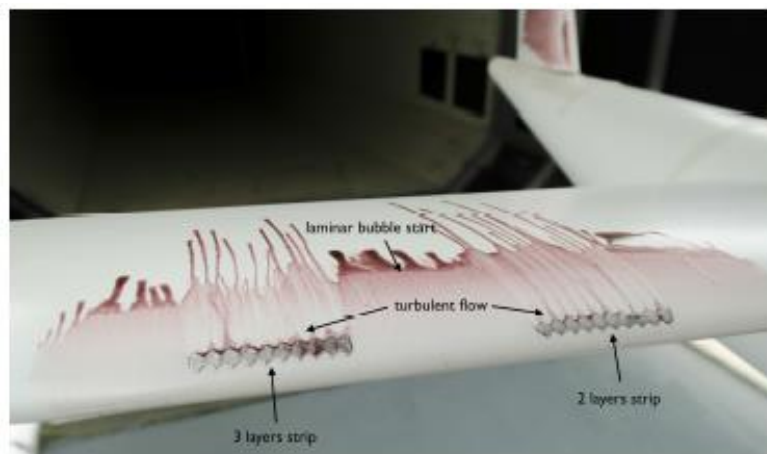


Fig 3. 13 – Flow visualization on wing

3.5.2 Scale effect and trip strips

The term *scale effects* refers to differences that arise when the fluid dynamic dimensionless parameters, mainly the Reynolds number, are not the same in low speed wind tunnel tests and flight operations. Reynolds number is defined as

$$\text{Re} = \frac{\rho V c}{\mu} \quad (3.10)$$

where ρ is the air density, V is the air speed, c is the wing mean aerodynamic chord (which is the reference length) and μ is the viscosity of the air. For the model investigated $c = 0.182$ m and all tests have been performed at a wind speed of about 40 m/s (the maximum available wind speed is about 50 m/s) with a Reynolds number of about 500 000.

For a large turbopropeller aircraft, the characteristic wing chord c is between 2.5 and 3.0 m, while the entire aircraft can be 30 m long. It is clear that full Reynolds number are not easily achievable in a wind tunnel, also because of power requirements (see again Tab 3.1), unless the air temperature is decreased to reduce its viscosity and the total pressure is increased to arise the air density, as done in high speed wind tunnels. Since the Reynolds number of low-speed wind tunnels cannot be the same of flight conditions, other artifices are needed to replicate the boundary layer of the full scale aircraft, otherwise laminar separations will affect the measurements. A simple and effective mean to comply with this need is the *trip strip*, which is an artificial roughness added to the model to fix the location of the transition from a laminar to turbulent boundary layer on the model. A correct installation prevents the realization of laminar bubbles and their consequences on the aerodynamic behaviour of the model. Trip strips made of adhesive tape with triangular edges have been placed on all components of the aircraft in order to promote the transition of the flow. The thickness and the right position of the trip strips has been estimated by tests of flow visualization through the use of fluorescent oil, as shown in Fig 3.12 and Fig. 3.13. Results lead to the conclusion that two layers of tape are sufficient to get the boundary layer transition at the desired place. The location of the trip strips is at about 5% local chord for wing and horizontal tail, even closer to the leading edge for the vertical tail, whereas they have been placed at 20% nose length on the fuselage.

3.6 WIND TUNNEL CORRECTIONS

In wind tunnel testing there are some constraints due by the nature of the tunnel itself. While there is no difference in having the model at rest and the air moving around it, the distances of some or all of the stream boundaries from the article under test are usually less than the corresponding distances for actual operations. In addition, the flow properties in the test section may not be the same in space and time. To include appropriate corrections, the following effects must be considered:

- **Horizontal buoyancy.** It refers to a variation of static pressure along the test section when no model is present. It produces a drag force analogous to the hydrostatic force on objects in a stationary fluid in a uniform gravitational field.

- **Solid blockage.** It is linked to the volume occupied by the model in the test section. This is the most influent effect, since it produces a variation in oncoming dynamic pressure. Essentially, the wind tunnel is a tube where the model in the test section “chokes” the flow. This effect produces surface stresses larger than the corresponding free-air operations. The stress distribution is assumed to be unchanged.

- **Wake blockage.** Every body immersed in a moving fluid has a wake, which size is function of the body shape and (in wind tunnel testing) of the ratio between the wake area and the tunnel area. The wake has a mean velocity lower than the free stream. According to the law of continuity, the velocity outside the wake in a closed tunnel must be higher than the free stream. By Bernoulli’s principle, the higher velocity in the main stream has a lowered pressure. As the boundary layer on the model (which later becomes the wake) grows, the model is put in a pressure gradient, hence there is a velocity increment on the model.

- **Streamlines curvature.** It refers to an alteration to the curvature of the streamlines of the flow about a body in a wind tunnel as compared to the corresponding curvature in an infinite stream. In a closed tunnel, the lift, pitching moment, hinge moments, and angle of attack are increased.

- **Normal downwash change.** It refers to the component of induced flow in the lift direction at the test article and it is due to the finite distances to the boundaries. In a closed jet, the lift produced is too large and the drag too small at a given geometric angle of attack, corresponding to a smaller downwash.

- **Spanwise downwash distortion.** It refers to an alteration to the local angle of attack along the span of a lifting wing. In a closed test section the angle of attack near the wingtips of a model with large span are increased, making the tip stall start at a lower geometric angle of attack. This effect becomes negligible if the model span is less than 0.8 the tunnel width.

- **Tail downwash change.** It refers to an alteration to the normal downwash behind the wing, so that the static stability is unnaturally increased.

These effects, in particular the solid blockage and the wake blockage, have been assessed for the model in all configurations and inserted in the wind tunnel software to have in output both the corrected and uncorrected values.

The solid blockage coefficients useful to apply the wind tunnel corrections has been determined on the basis of the aircraft components volumes as suggested by Barlow, Rae, and Pope (Ref [6]).

CHAPTER 4 - WIND TUNNEL TESTS

4.1 REFERENCE SYSTEM

Before describing the tests, it is essential to define the conventions of the coefficients signs on the basis of the reference system adopted.

The reference system more comfortable for our work is that shown in the Fig 4.1. The x-y-z axes are fixed to the aircraft with the origin in the reference point or *pole* (point placed at 25% of the wing mean aerodynamic chord, when the wing is in the middle position on the fuselage):

- The x-axes is placed in the plane of symmetry and its positive direction is towards the fuselage tail.
- The y-axes is perpendicular to the plane of the symmetry and directed towards the right wing of the model.
- The z-axes is perpendicular to the other two, positive upward.

As mentioned in the section 3.3.1 the sideslip angle is assumed to be positive in sign when the airflow comes from the left wing the model. (This is the opposite of the usual convention).

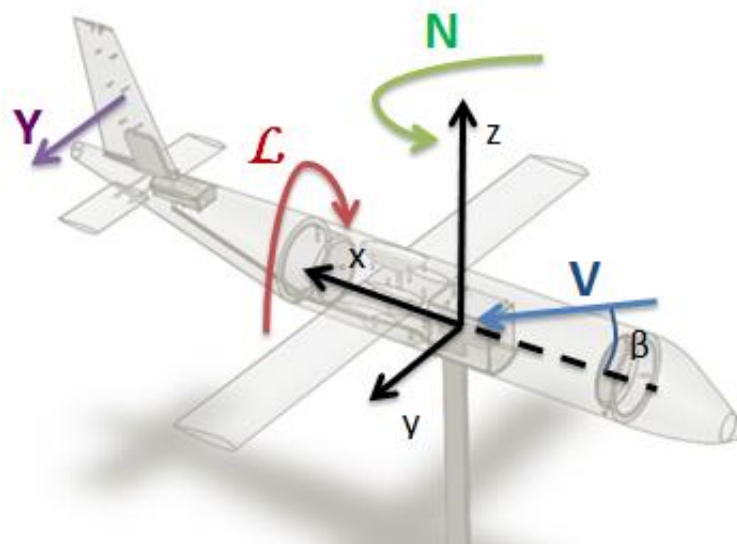


Fig 4. 1 – Reference system

4.2 TEST PROCEDURE

The typical experimental test is structured as follow:

- Setup of the configuration
- Data acquisition
- Data elaboration and storage

4.1.1 Setup of the configuration

The test's list has also been made in order to switch among configurations in a short time. The objective is to consider partial aircraft configurations and subsequently the complete aircraft configuration in order to provide data about aerodynamics interference among aircraft components in sideslip condition.

4.1.2 Data acquisition

The data acquisition procedure is stepped as follows:

- The tunnel is set on and led to the operative conditions.
- The model is set at the zero sideslip condition. The operator acquires the data at each attitude after a waiting time of about 3 second to grant a stationary condition of the flow. The acquisition software samples data at 100 Hz, printing at video the mean value of the last 200 acquired data.
- Once the zero sideslip conditions have been acquired, the model is turned at the about -6° sideslip with a step of 2° . Subsequently the operator brings back the model to the initial attitude and the sampling continues till the sideslip angle of about $+12^\circ$, with a sampling step of about 2° . During a test the operator must monitor values of the sideslip angle on the PC and on a special bearing scale positioned on the floor of the test chamber.

4.1.3 Data elaboration and storage

The aerodynamic force and moment coefficients are calculated by the acquired measurement of forces and dynamic pressures.

To these coefficients two different corrections have been applied:

- **Wind tunnel corrections.** As already discussed in section 3.6, the wind tunnel walls presence produce a lateral constraint to the flow pattern about the body, this is known as solid blockage. The solid blockage leads to an increase of the dynamic pressure, increasing all forces and moment at a given sideslip angle. Wind tunnel walls produce also a constraint for the wake, known as wake blockage, which increases with the wake size. In Tab 4.1 are reported solid blockage and wake blockage coefficients useful to apply the wind tunnel corrections.

Solid blockage for combinations			
Config.	V Av 1.0	V Av 1.5	V Av 2.0
BV	0.010219	0.010257	0.010281
WBV	0.011272	0.011310	0.011334
WBVH	0.011411	0.011449	0.011473
BVH	0.010358	0.010395	0.010419
WB	0.011114	0.011114	0.011114

Wake blockage for combinations			
Config.	V Av 1.0	V Av 1.5	V Av 2.0
BV	0.000051	0.000070	0.000085
WBV	0.000764	0.000775	0.000783
WBVH	0.000839	0.000850	0.000858
BVH	0.000093	0.000095	0.000097
WB	0.000730	0.000730	0.000730

Tab. 4. 1 – Solid and wake blockage coefficients for the wind tunnel corrections.

- **Moments transfer.** The point placed at 25% of the wing mean aerodynamic chord, when the wing is in the middle position on the fuselage, has been chosen as the reference point for the calculation of the aerodynamic forces and moments. Since the balance center does not coincide with the chosen reference point, the aerodynamic moments must be transferred to the desired reference point.

Fig 4.2 schematically illustrates the location of the reference point, its distances from the balance center and the distances of the aerodynamic center of the various vertical tails investigated from the balance center.

The transfer of the rolling and yawing moment from the balance center to the chosen reference point can be expressed as shown in Eq 4.1 and Eq. 4.2:

$$N_{pole} = N_{cb} + F_y \cdot \Delta x \quad (4.1)$$

$$\mathcal{L}_{pole} = \mathcal{L}_{cb} + F_y \cdot \Delta z \quad (4.2)$$

where the quantities $\Delta x = -199.30$ mm and $\Delta z = 30.60$ mm are the longitudinal and vertical distances of the chosen reference point from the balance center respectively.

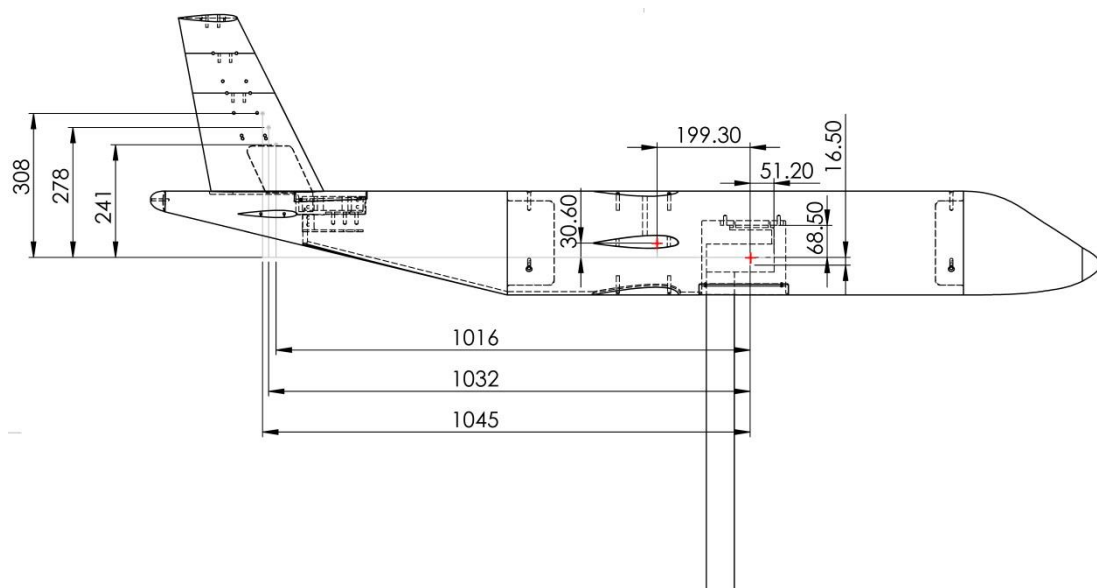


Fig 4. 2 – Location of the reference point

4.3 THE EXPERIMENTAL TESTS CAMPAIGN

4.3.1 Preliminary tests

The preliminary tests is for the valuation of the scale effects. As already discussed in the section 3.6, trip strips have been placed on all components of the aircraft in order to promote the transition of the flow. Transitional strips have been placed about 5% of local chord, both on the lower and upper surface, for wing and horizontal tail, even closer to the leading edge for the vertical tail, whereas they have been placed at 20% nose length on the fuselage. The thickness adopted is about 0.2 mm (two layers of tape).

Fig 4.3 show the effects of the trip strips on the global yawing moment coefficient at two different values of velocity.

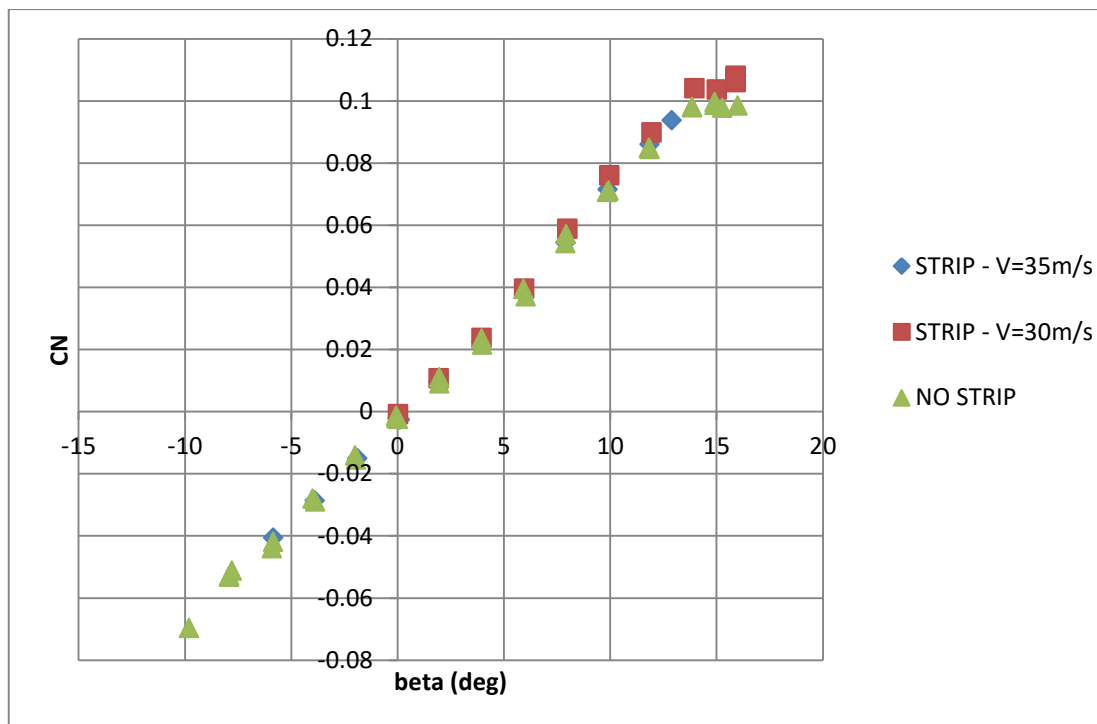


Fig 4. 3 – Preliminary tests (Trip strips)

4.3.2 Configurations results

The results were collected from 49 configurations that include two different positions of the wing respect to the fuselage (high and low wing), variation in shape of the vertical tail's planform and variations of the position of the horizontal plane. The experimental tests campaign involved only the fuselage tail cone with the parameter $(z_{fc}/r_f)=1$, symbolically indicated as Body High (BH).

The vertical tails have been labeled as V10, V15 V20 according to the aspect ratio value, $AR_v=1.0$, $AR_v=1.5$ and $AR_v=2.0$.

The wing's position respect to the fuselage has been labeled as WH (Wing high) or WL (Wing Low).

The position of the horizontal plane has been labeled according to the figure 4.3, where H5 identifies the T-tail configuration, H2, H3 and H4 identify the cruciform configurations while H1 identifies the body mounted tail configuration. (The cruciform configuration H2 was planned only for the vertical tail with $AR_v=2.0$).

The Fig 4.5 shows the configuration with high wing, vertical tail of $AR_v=20$ and T-empennage. According to the notation above mentioned it is labeled with the ID: BH_WH_V20_H5

For each configuration the yawing moment coefficient, the rolling moment coefficient, and the lateral-directional stability derivatives has been measured.

All the tested configurations, together with lateral-directional stability derivatives are shown in the Tab 4.2 .

Thanks to the adoption of the off-center load cell, it was measured also the contribute of the vertical tailplane on the directional stability derivative.

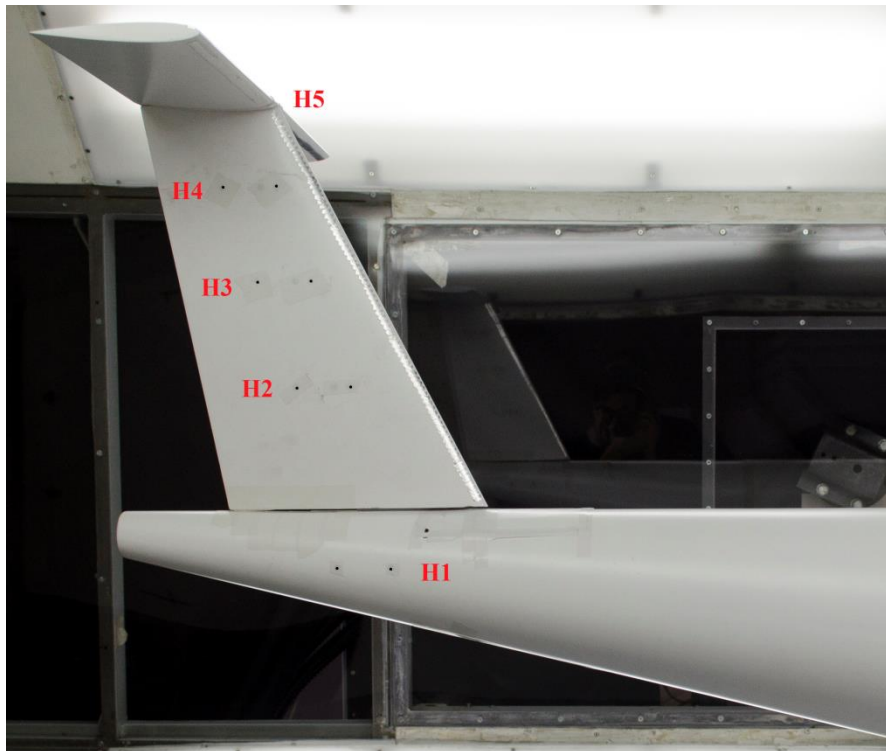


Fig 4. 4 – Positions of the horizontal plane.

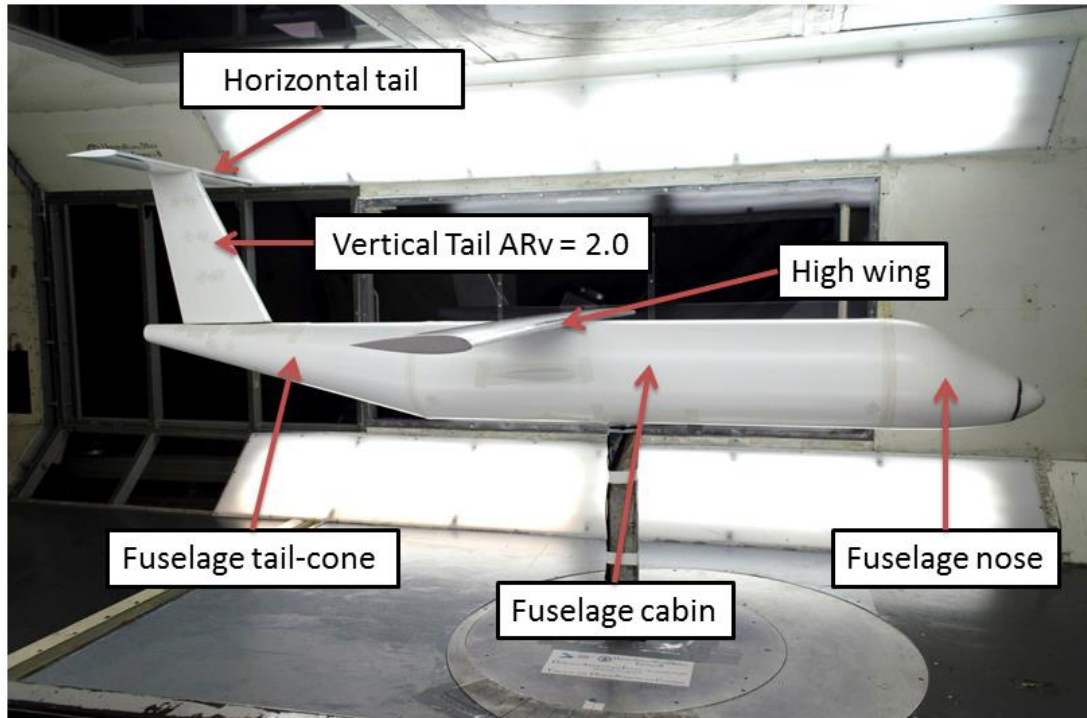


Fig 4. 5 – BH_WH_V20_H5 configuration

Tab. 4. 2 – Configurations results

ID	CONFIGURATION	CN β (1/deg)	C $L\beta$ (1/deg)	CN β_v (1/deg)
BH	Body high	-0.0031	0.0001	0.0000
BH_V10	Body high Vert. AR=1	0.0004	-0.0008	0.0031
BH_V15	Body high Vert. AR=1.5	0.0026	-0.0014	0.0052
BH_V20	Body high Vert. AR=2	0.0045	-0.0029	0.0071
BH_V10_H1	Body high Vert. AR=1 Horiz. pos1	0.0012	-0.0006	0.0037
BH_V10_H3	Body high Vert. AR=1 Horiz. pos3	0.0006	-0.0008	0.0031
BH_V10_H4	Body high Vert. AR=1 Horiz. pos4	0.0010	-0.0010	0.0036
BH_V10_H5	Body high Vert. AR=1 Horiz. pos5	0.0017	-0.0013	0.0042
BH_V15_H1	Body high Vert. AR=1.5 Horiz. pos1	0.0037	-0.0014	0.0060
BH_V15_H3	Body high Vert. AR=1.5 Horiz. pos3	0.0025	-0.0023	0.0051
BH_V15_H4	Body high Vert. AR=1.5 Horiz. pos4	0.0029	-0.0018	0.0054
BH_V15_H5	Body high Vert. AR=1.5 Horiz. pos5	0.0040	-0.0022	0.0064
BH_V20_H1	Body high Vert. AR=2 Horiz. pos1	0.0055	-0.0032	0.0079
BH_V20_H2	Body high Vert. AR=2 Horiz. pos2	0.0043	-0.0022	0.0068
BH_V20_H3	Body high Vert. AR=2 Horiz. pos3	0.0044	-0.0024	0.0069
BH_V20_H4	Body high Vert. AR=2 Horiz. pos4	0.0040	-0.0027	0.0066
BH_V20_H5	Body high Vert. AR=2 Horiz. pos5	0.0052	-0.0032	0.0077
BH_WH_V10	Wing high Body high Vert. AR=1	0.0002	-0.0014	0.0031
BH_WH_V10_H1	Wing high Body high Vert. AR=1 Horiz. pos1	0.0010	-0.0013	0.0036
BH_WH_V10_H3	Wing high Body high Vert. AR=1 Horiz. pos3	0.0001	-0.0015	0.0030
BH_WH_V10_H4	Wing high Body high Vert. AR=1 Horiz. pos4	0.0005	-0.0017	0.0034
BH_WH_V10_H5	Wing high Body high Vert. AR=1 Horiz. pos5	0.0012	-0.0020	0.0041
BH_WH_V15	Wing high Body high Vert. AR=1.5	0.0021	-0.0020	0.0050
BH_WH_V15_H1	Wing high Body high Vert. AR=1.5 Horiz. pos1	0.0034	-0.0025	0.0059
BH_WH_V15_H3	Wing high Body high Vert. AR=1.5 Horiz. pos3	0.0022	-0.0021	0.0051
BH_WH_V15_H4	Wing high Body high Vert. AR=1.5 Horiz. pos4	0.0017	-0.0020	0.0045
BH_WH_V15_H5	Wing high Body high Vert. AR=1.5 Horiz. pos5	0.0035	-0.0029	0.0064
BH_WH_V20	Wing high Body high Vert. AR=2	0.0040	-0.0034	0.0069
BH_WH_V20_H1	Wing high Body high Vert. AR=2 Horiz. pos1	0.0054	-0.0034	0.0079
BH_WH_V20_H2	Wing high Body high Vert. AR=2 Horiz. pos2	0.0039	-0.0030	0.0067

BH_WH_V20_H3	Wing high Body high Vert. AR=2 Horiz. pos3	0.0039	-0.0035	0.0068
BH_WH_V20_H4	Wing high Body high Vert. AR=2 Horiz. pos4	0.0042	-0.0038	0.0071
BH_WH_V20_H5	Wing high Body high Vert. AR=2 Horiz. pos5	0.0051	-0.0047	0.0079
BH_WL_V10	Wing low Body high Vert. AR=1	0.0009	0.0008	0.0033
BH_WL_V10_H1	Wing low Body high Vert. AR=1 Horiz. pos1	0.0016	0.0008	0.0038
BH_WL_V10_H3	Wing low Body high Vert. AR=1 Horiz. pos3	0.0010	0.0006	0.0032
BH_WL_V10_H4	Wing low Body high Vert. AR=1 Horiz. pos4	0.0014	0.0004	0.0037
BH_WL_V10_H5	Wing low Body high Vert. AR=1 Horiz. pos5	0.0021	0.0000	0.0044
BH_WL_V15	Wing low Body high Vert. AR=1.5	0.0030	-0.0004	0.0053
BH_WL_V15_H1	Wing low Body high Vert. AR=1.5 Horiz. pos1	0.0041	-0.0001	0.0062
BH_WL_V15_H3	Wing low Body high Vert. AR=1.5 Horiz. pos3	0.0031	-0.0003	0.0053
BH_WL_V15_H4	Wing low Body high Vert. AR=1.5 Horiz. pos4	0.0029	-0.0003	0.0051
BH_WL_V15_H5	Wing low Body high Vert. AR=1.5 Horiz. pos5	0.0044	-0.0015	0.0066
BH_WL_V20	Wing low Body high Vert. AR=2	0.0051	-0.0013	0.0074
BH_WL_V20_H1	Wing low Body high Vert. AR=2 Horiz. pos1	0.0062	-0.0020	0.0083
BH_WL_V20_H2	Wing low Body high Vert. AR=2 Horiz. pos2	0.0049	-0.0018	0.0072
BH_WL_V20_H3	Wing low Body high Vert. AR=2 Horiz. pos3	0.0051	-0.0012	0.0073
BH_WL_V20_H4	Wing low Body high Vert. AR=2 Horiz. pos4	0.0048	-0.0018	0.0071
BH_WL_V20_H5	Wing low Body high Vert. AR=2 Horiz. pos5	0.0066	-0.0027	0.0087

After the list of the tested configurations it is interesting to compare the trend of the yawing moment coefficient, the rolling moment coefficient and the yawing moment coefficient for isolated fuselage, a body-vertical tail configuration and this latter configuration with also the horizontal tail..

The body isolated is shown in the Fig 4.6 a).

The body-vertical chosen configuration is BH_V15 and is shown in Fig 4.6 b).

For these latter we have considered the body mounted tail configuration that is labeled with ID: BH_V15_H1 and is shown in the Fig 4.6 c).

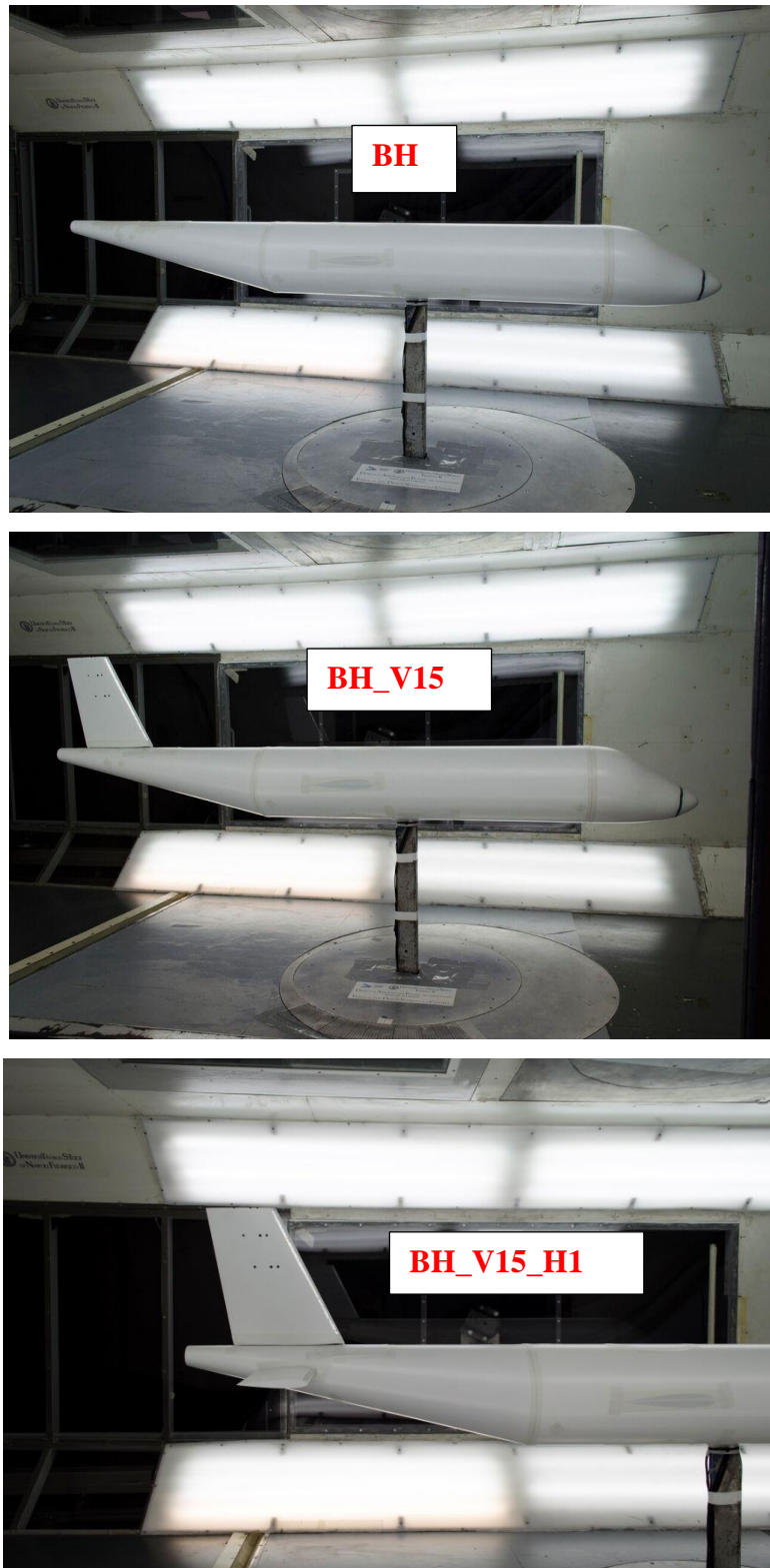


Fig 4. 6 – a) BH; b) BH_V15; c) BH_V15_H1

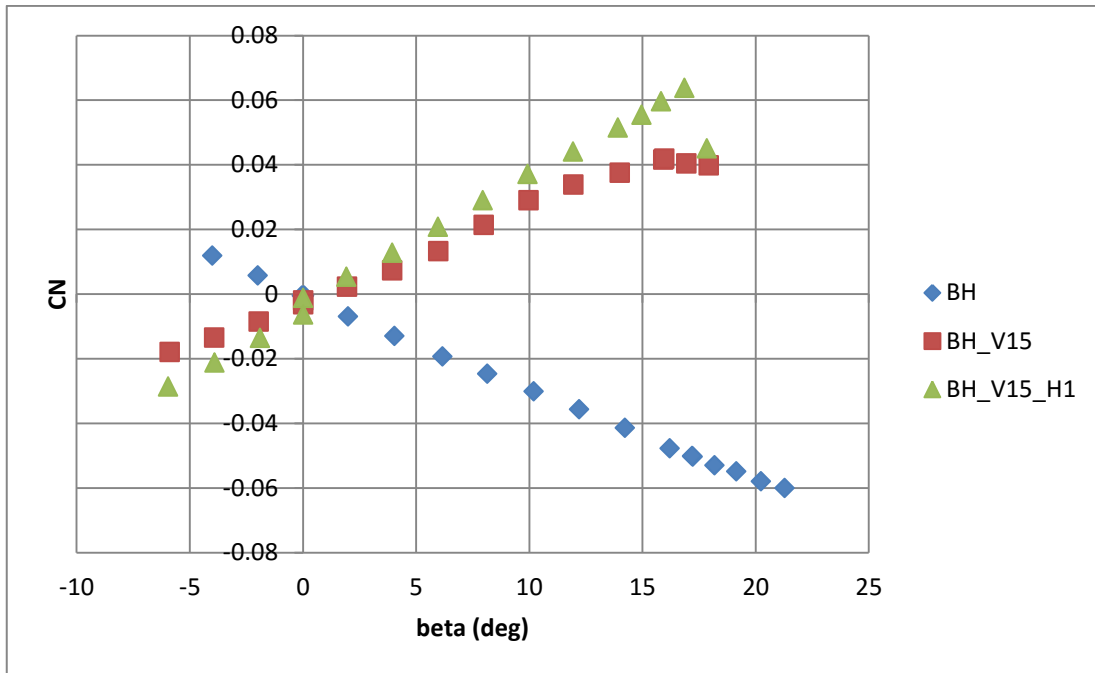


Fig 4. 7 – CN versus β

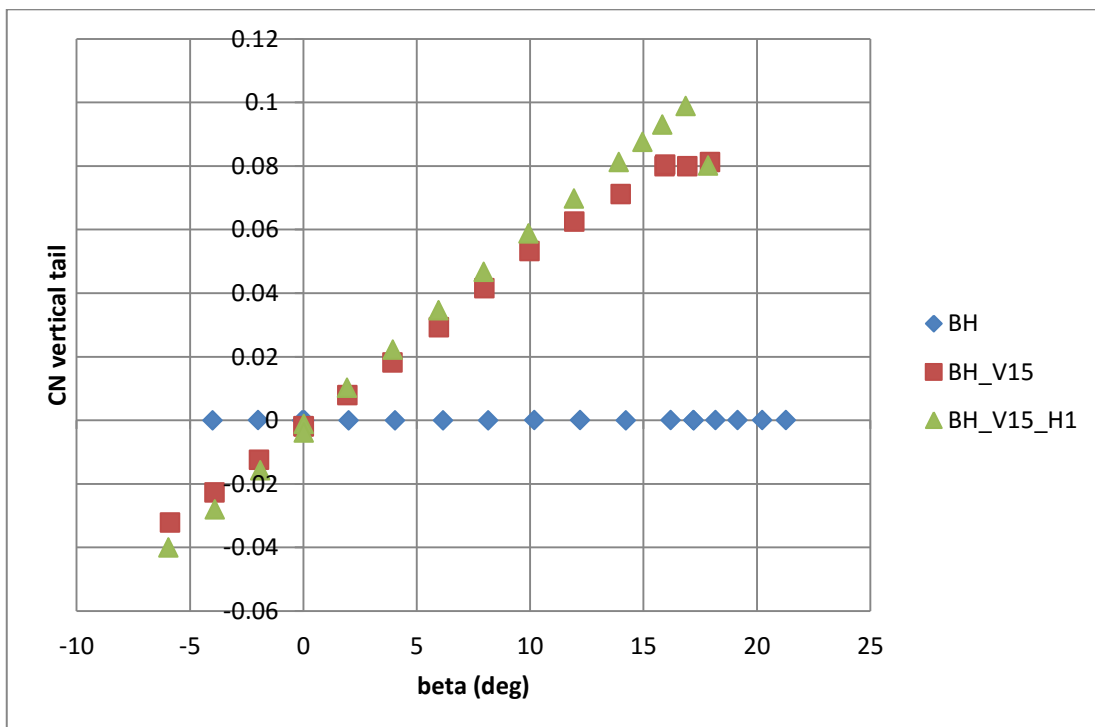


Fig 4. 8 – CN_{vertical} versus β

The Fig 4.7 highlight that the fuselage is unstable to the directional stability (the slope of the curve of the CN for the isolated body is negative).

The body vertical configuration is stable thanks to the introduction of the vertical tail that plays the role of the stabilizing surface. The transition from BV to BVH increases the directional stability, in fact the slope of the curve is positive and more strong that the previous case.

This effects is more clear in the Fig 4.8 which reports the yawing moment coefficient measured only by the off-center load cell. It highlight the aerodynamics interference of the horizontal tail on the vertical tail.

The Fig. 4.9 shows the rolling moment coefficient versus sideslip angle for the above mentioned configurations.

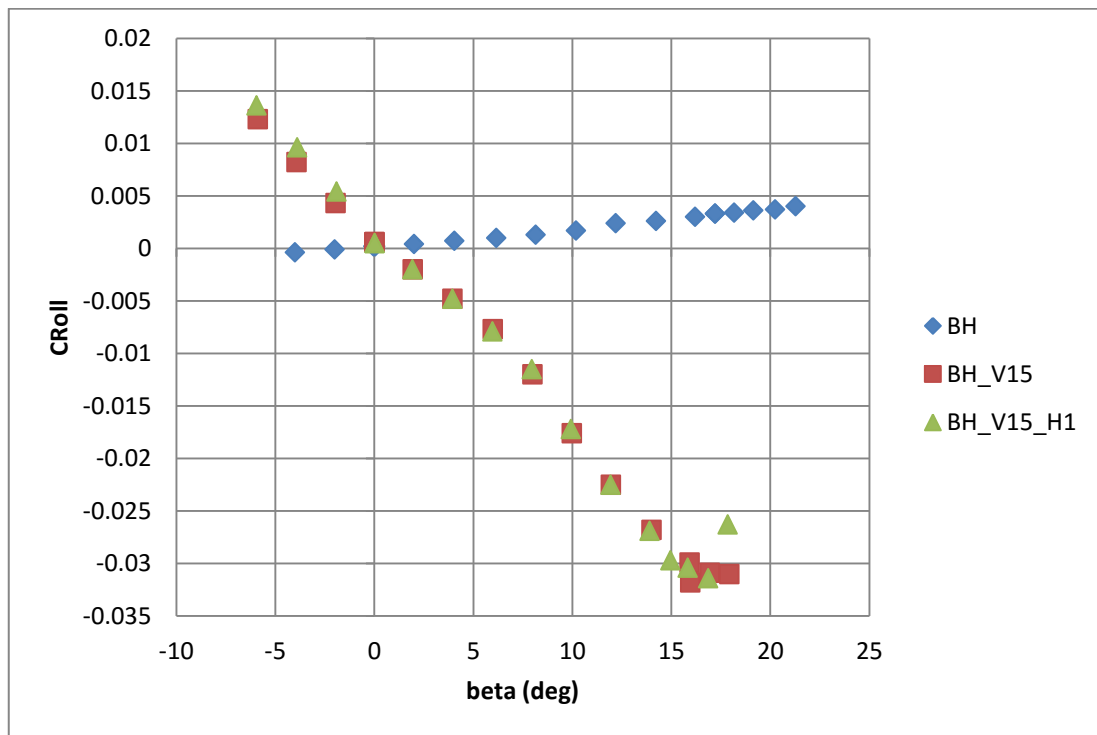


Fig 4. 9 – Croll versus β

It is now interesting evaluate the effect of the wing on the yawing moment coefficient curve and on the rolling moment coefficient curve.

The Fig 4.10 and 4.11 show the configurations BH_WH_V15_H1 and BH_WL_V15_H1.

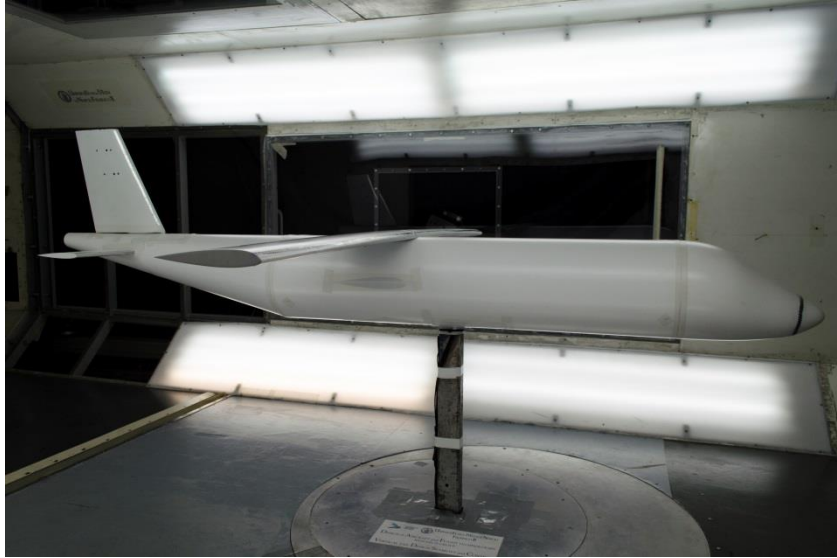


Fig 4. 10 - BH_WH_V15_H1



Fig 4. 11 - BH_WL_V15_H1

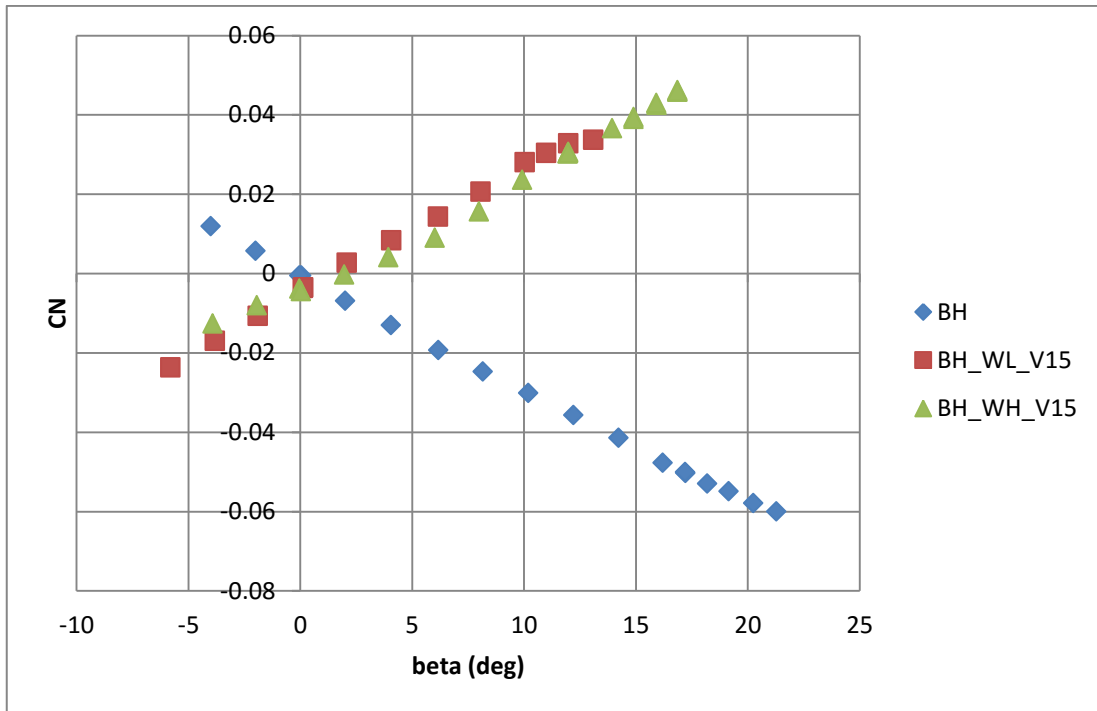


Fig 4. 12 – CN versus β for indicated configurations

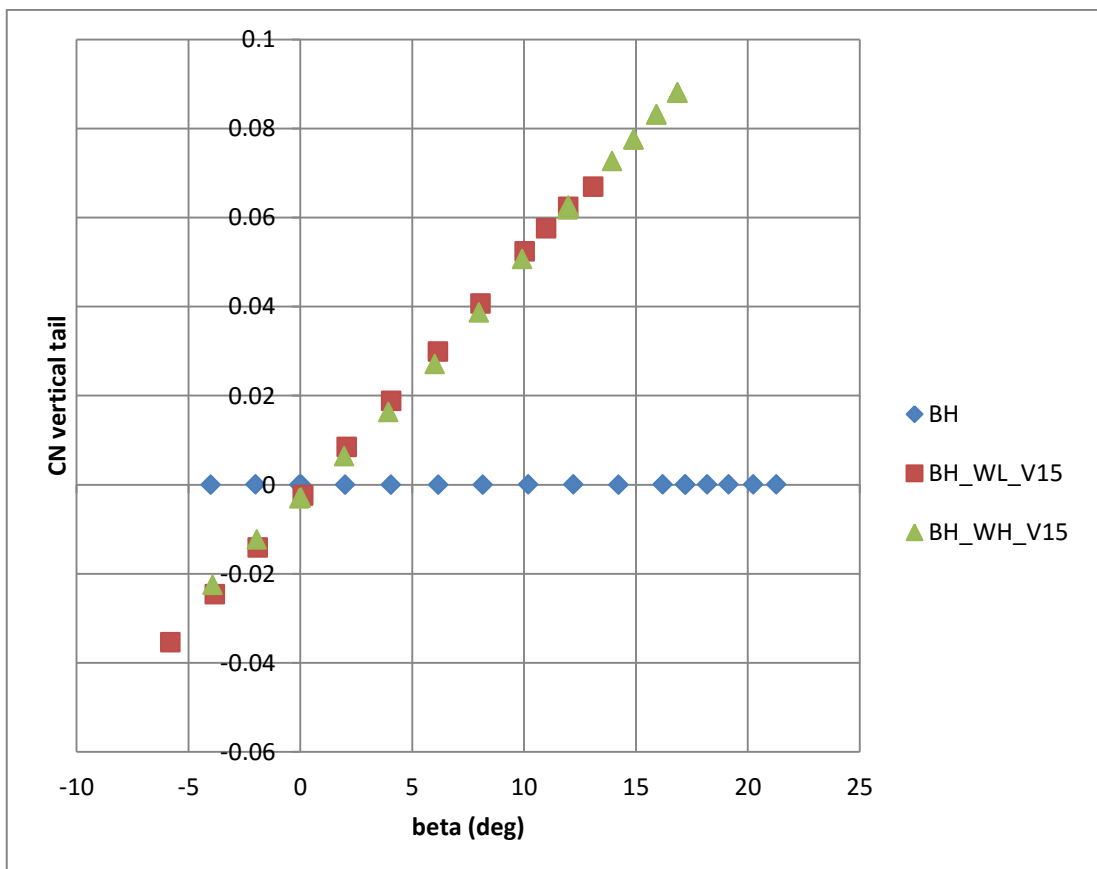


Fig 4. 13 – CN_v for indicated configurations

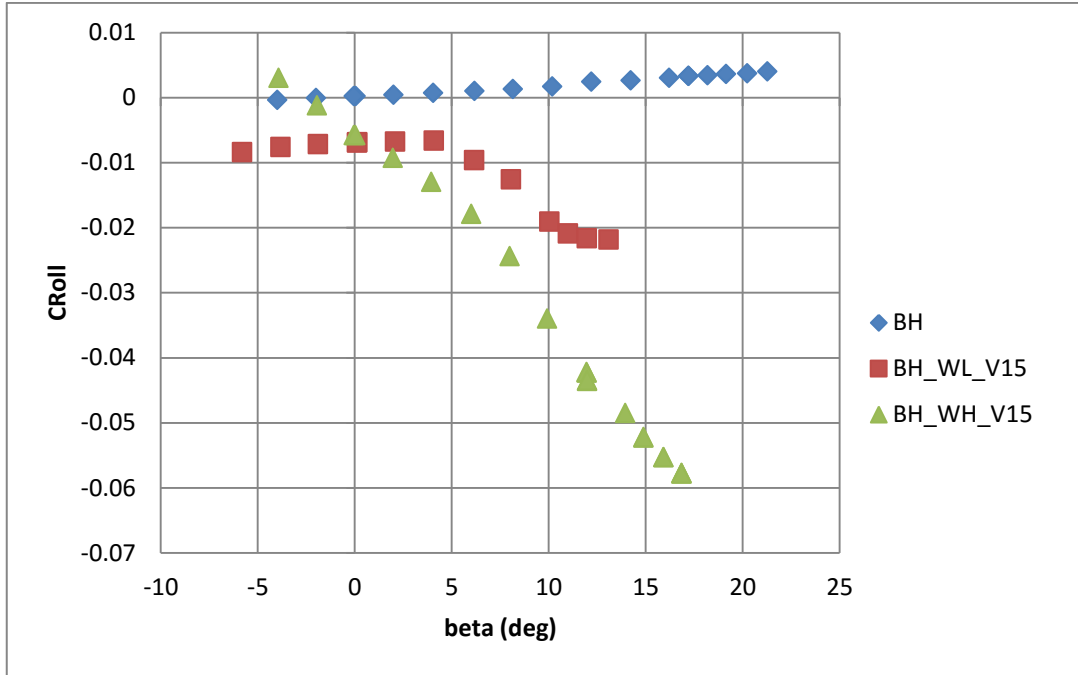


Fig 4. 14 . Croll versus β for indicated configurations

The Fig 4.16 and Fig 4.17 show the effect of the position of the wing on the yawing moment coefficient curve versus β and on the rolling moment coefficient curve versus β .

We can see that the complete configuration with low wing has the slope of the yawing moment coefficient curve positive and stronger than that of the same configuration but with high wing.

The configuration BH_WH_V15_H1 has more lateral static stability respect the configuration BH_WL_V15_H1. This phenomenon can be easily explained looking the Fig. 4.17 A) and B).

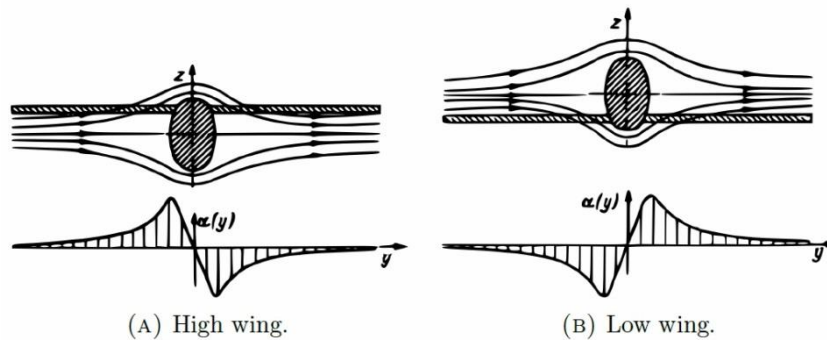


Fig 4. 15 – Effect of wing position respect the fuselage in sideslip conditions

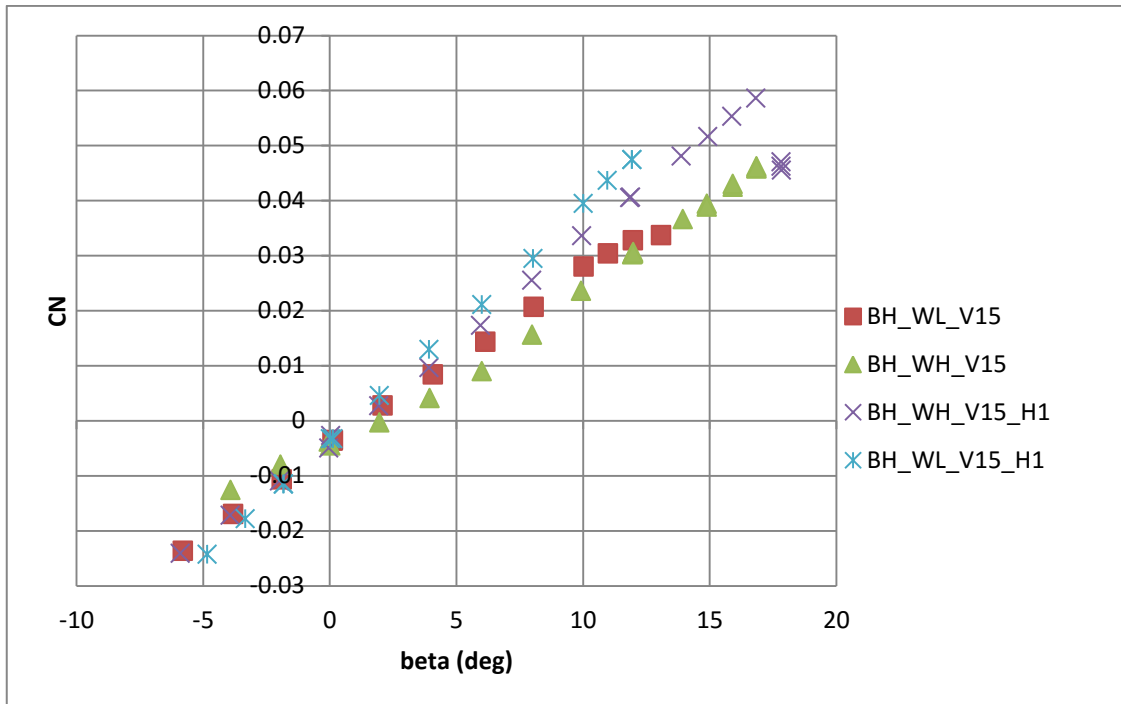


Fig 4. 16 – Effect of the wing position on the CN

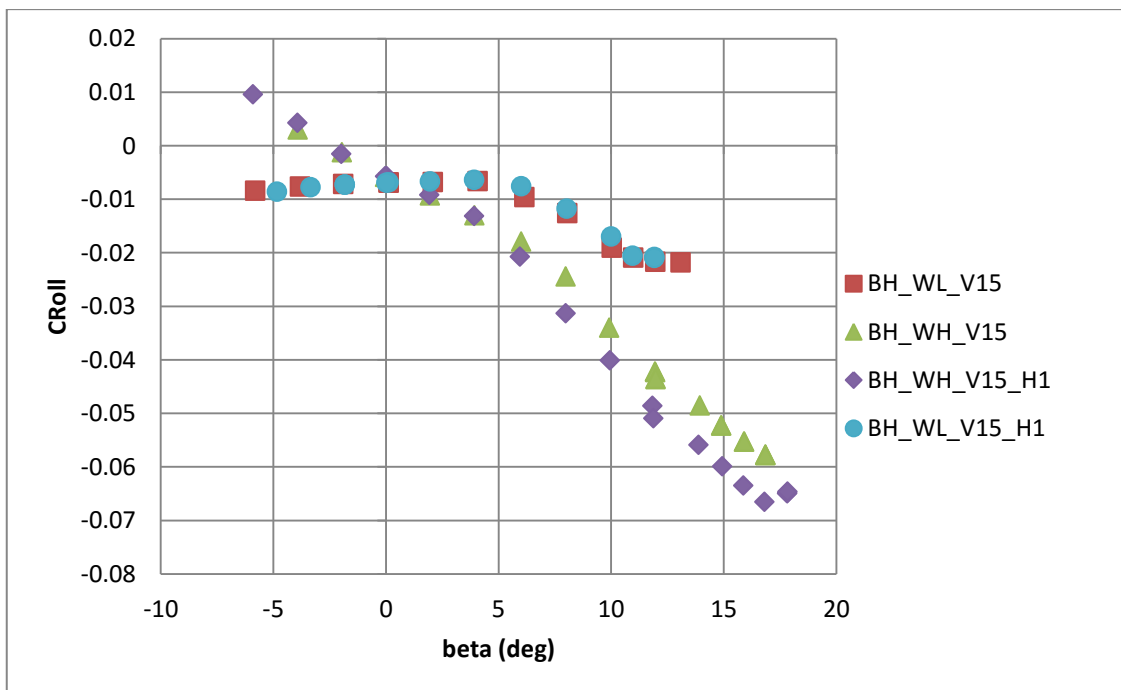


Fig 4. 17 – Effect of the wing position on the CRoll

4.3.3 Mutual aerodynamic interference effect

Body-vertical tail mutual interference effects

It is particularly important show the mutual interference effects between fuselage and vertical tail in sideslip condition. For this scope we have tested in wind tunnel the isolated fuselage and the combination body-vertical varying the aspect ratio AR_v .



Fig 4. 18 – BH_V10



Fig 4. 19 – BH_V15



Fig 4. 20 – BH_V20

The Fig 4.21 and 4.22 show the mutual aerodynamic interference between body and vertical tail in sideslip condition.

More in details the Fig 4.21 reports the trend of the indicated derivatives varying the aspect ratio of the vertical tail.

The Fig 4.22 shows the effect of the fuselage on the vertical tail in sideslip and the effect of the vertical tail plane on the fuselage in sideslip. The geometric parameter governing this factor is the ratio of the vertical tail span b_v to fuselage height d_{fv} , representing the relative size between the vertical stabilizer and the fuselage section (see Fig 4.23). The yawing moment coefficient of the isolated fuselage has been measured experimentally, while the yawing moment coefficient of the isolated vertical tailplane has been calculated semi empirical way with the formula of Helmbold-Diederich for the $C_{L_{\alpha v}}$ (see Fig 4.24). It is possible to note two results:

- There is an increase of vertical tail effectiveness in sideslip in almost all the configurations analyzed.
- The vertical tail plane reduces the fuselage instability in sideslip.

In the range of $\frac{b_v}{d_{fv}}$ from 2 to 4, the coupling between vertical tailplane and fuselage is beneficial for both. The vertical tail increase its effectiveness whereas the fuselage has reduced directional instability.

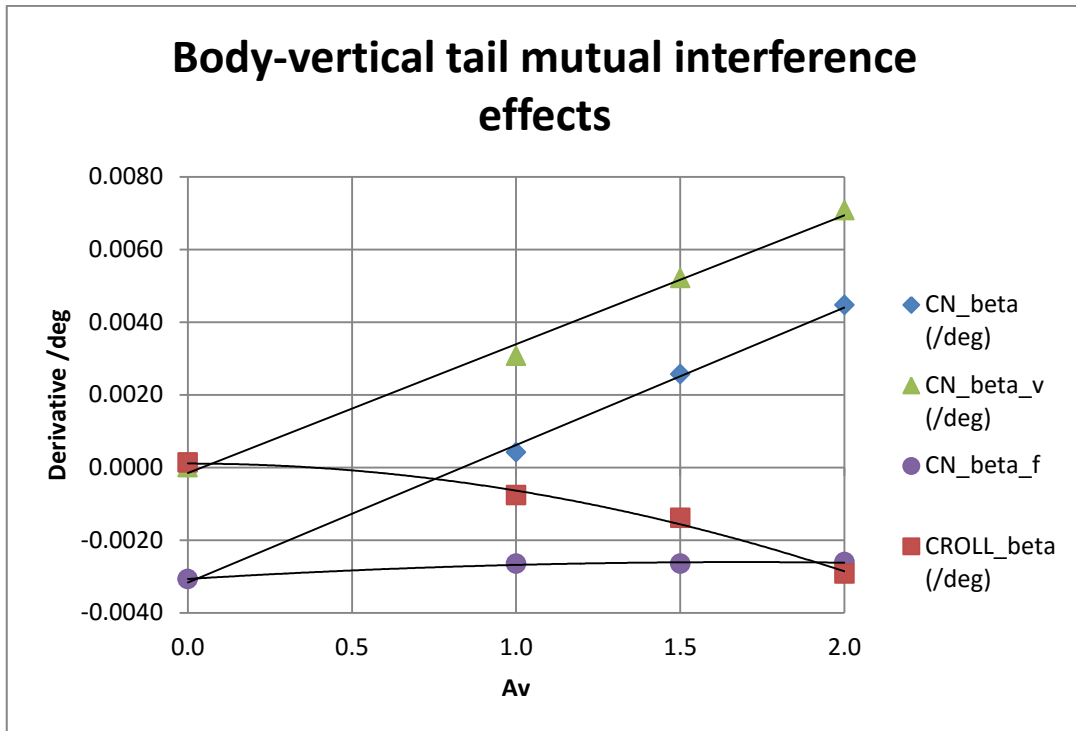


Fig 4. 21 – CN_beta and Croll_beta versus AR_v

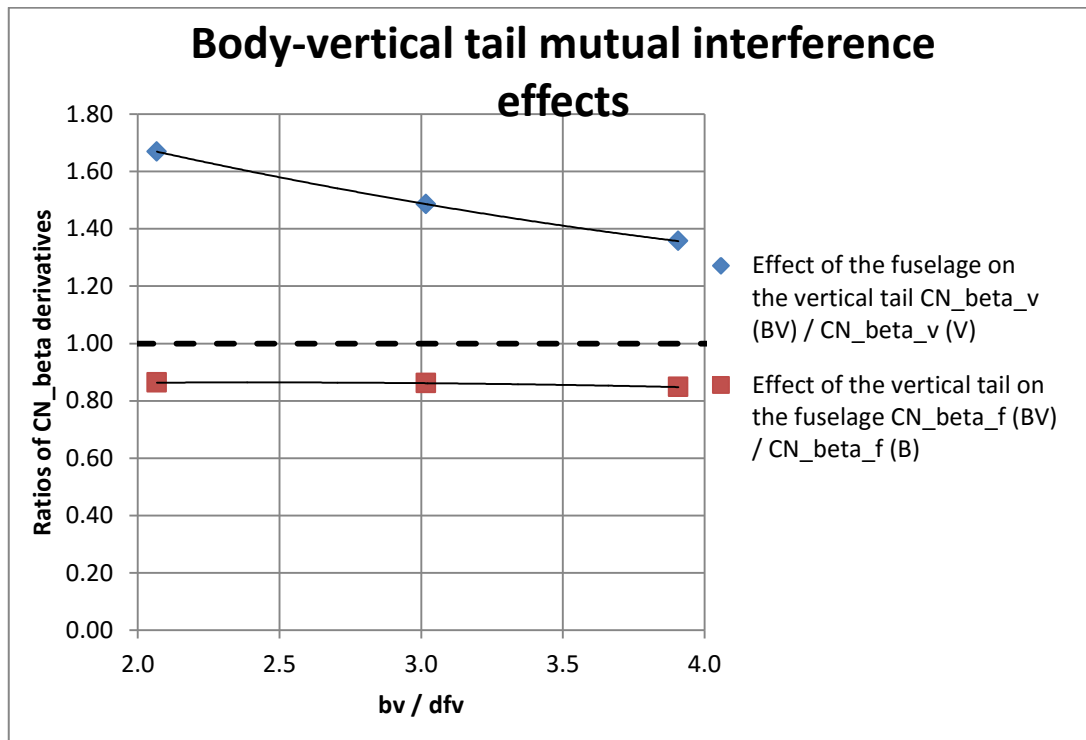


Fig 4. 22 – Interference factors

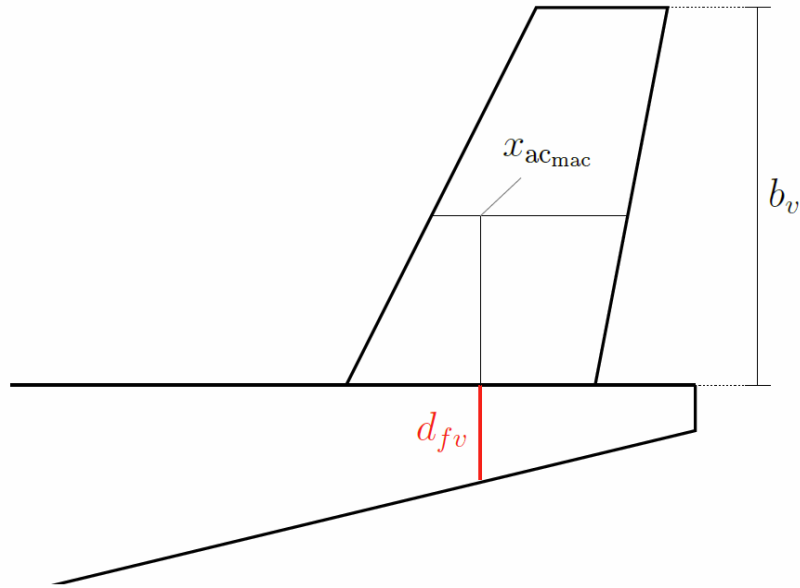


Fig 4. 23 – b_v/d_{fv}

$$C_{L_{\alpha_v}} = \frac{2\pi A_v}{2 + \sqrt{\frac{B^2 A_v^2}{\kappa^2} \left(1 + \frac{\tan^2 \Lambda_{v,c/2}}{B^2}\right) + 4}}$$

where

A_v is the vertical tail aspect ratio, b_v^2/S_v

B is the compressibility parameter, $\sqrt{(1 - M^2)}$

κ is the ratio of *section* lift-curve slope to theoretical thin-section value, $c_{l_{\alpha}}/(2\pi B)$, and for thin airfoils ($c_{l_{\alpha}} \approx 2\pi$) it is equal to $1/B$

$\Lambda_{v,c/2}$ is the vertical tail sweep angle at half chord.

Fig 4. 24 – Lift curve slope of the isolated vertical tailplane

Effect on the wing position – Wing interference

Another important effect is the effect of the wing sidewash on the vertical tailplane. The Fig 4.25 and 4.26 show some wing-body-vertical configurations investigated.

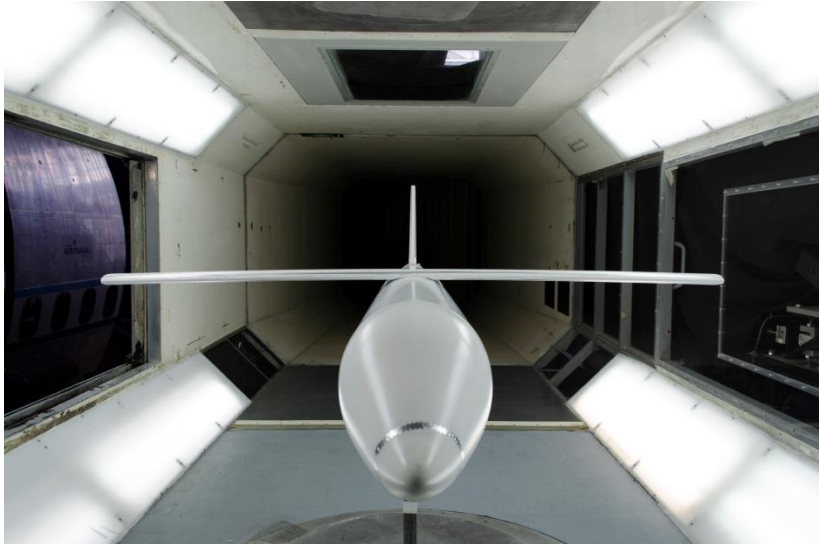


Fig 4. 25 – Example of WBV configuration with high wing



Fig 4. 26 – Example of WBV configuration with low wing

The Fig. 4.27 and 4.28 show the effect of the wing position on the total $C_{N\beta}$ and on the vertical tail $C_{N\beta V}$. For the fuselage tail cone investigated we can see a little increase of the effectiveness of the vertical tail plane in the case of low wing configuration and a little decrease in the case of high wing. To fix the wing position this effect is function of the aspect ratio AR_v .

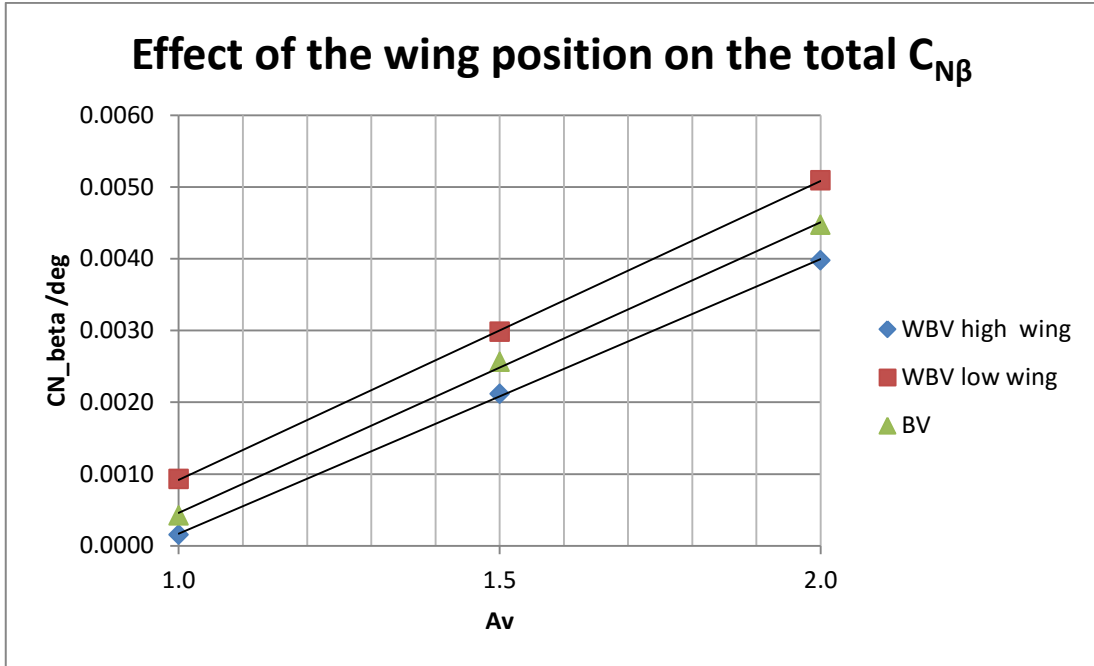


Fig 4. 27 – Effect wing position on $C_{N\beta}$

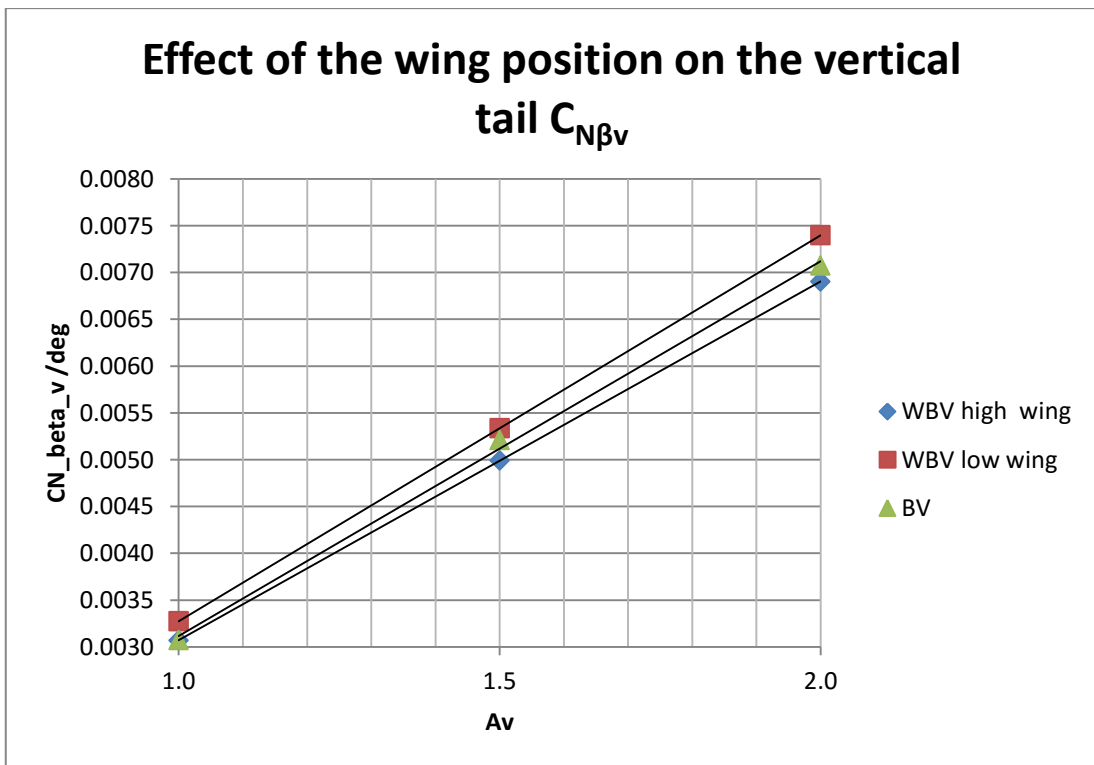


Fig 4. 28 - Effect wing position on $C_{N\beta v}$

Horizontal tailplane interference

The last effect is the horizontal tailplane interference. This effect is function of the wing position, of the aspect ratio AR_v (indicated as Av in the figures) and of the empennage configuration. This latter factor has been expressed by the parameter $\left(\frac{z_h}{b_v}\right)$ shown in the Fig. 4.29.

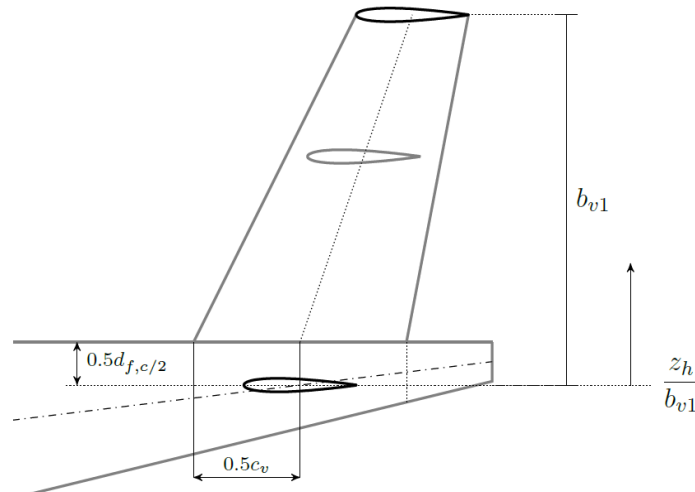
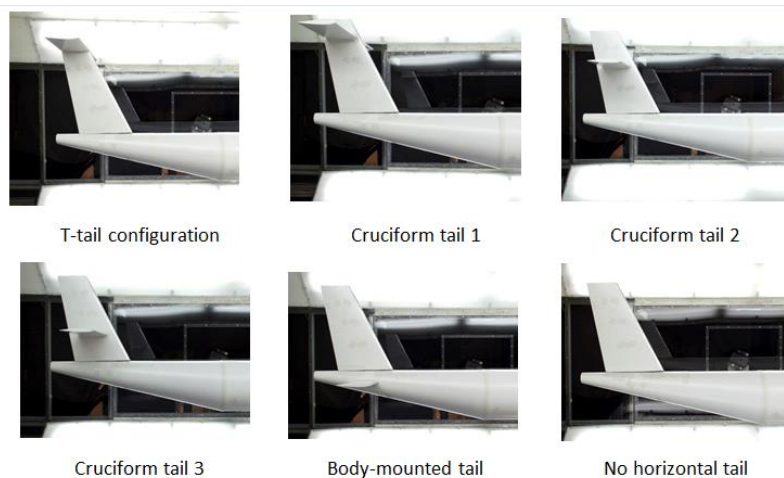


Fig 4. 29 - $\left(\frac{z_h}{b_v}\right)$ parameter

From the Fig 4.31 and 4.32 we can see that the horizontal tailplane increases the effectiveness of the vertical stabilizer in sideslip up to 45% in the case of the T-tail empennage configuration, whereas a cruciform empennage configuration decreases it up to 8%.

Fig 4. 30 – Empennage configurations



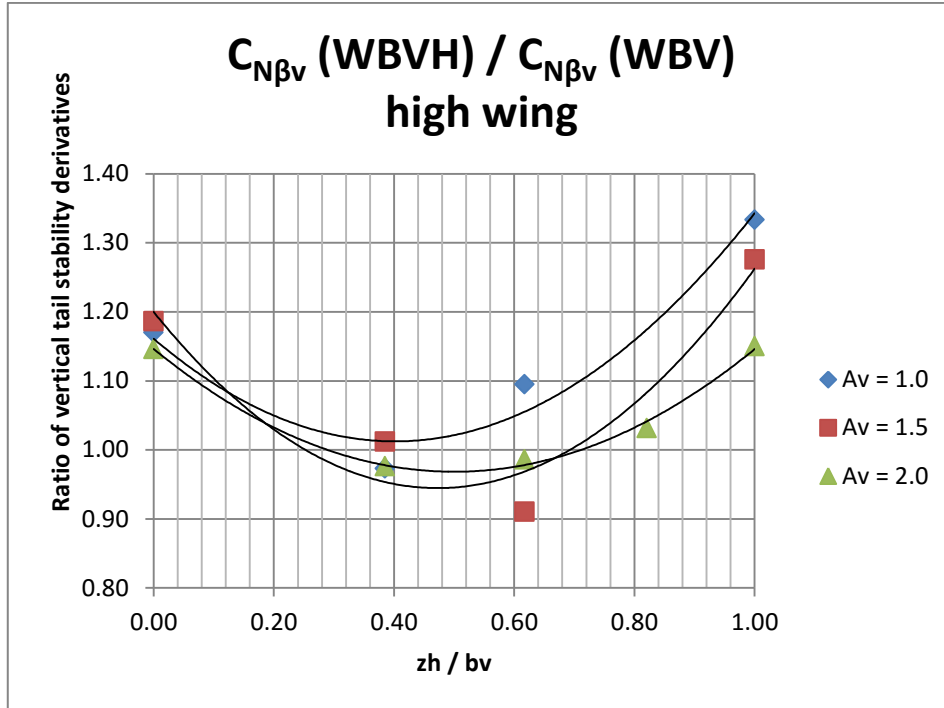


Fig 4. 31 – Aerodynamic interference factor due to the horizontal stabilizer on the vertical tailplane. (High wing)

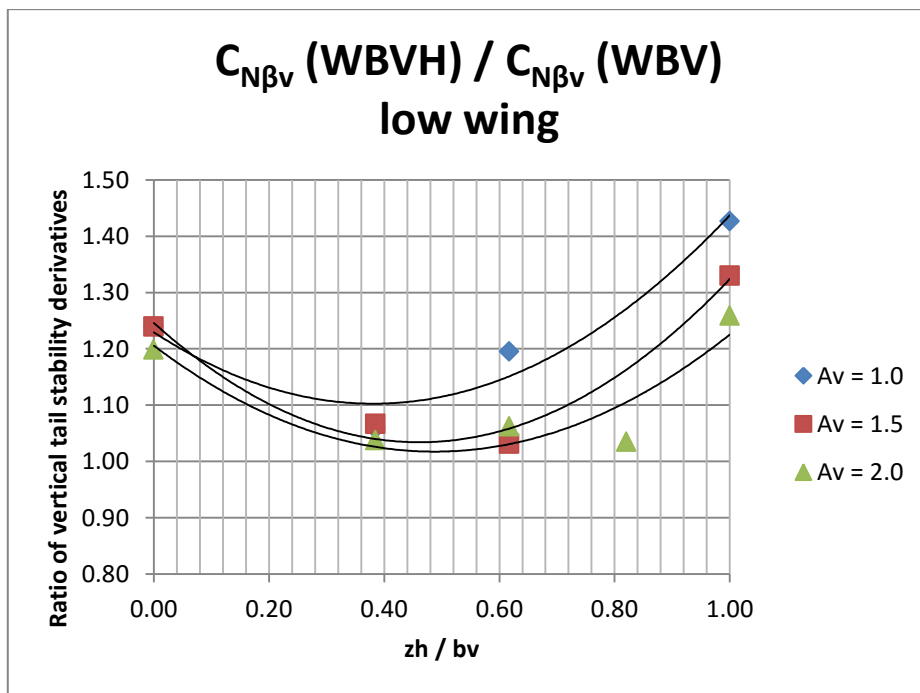


Fig 4. 32 – Aerodynamic interference factor due to the horizontal stabilizer on the vertical tailplane. (Low wing)

REFERENCES

- [1] C. D. Perkins, R.E. Hage. *Airplane performance stability and control*. Wiley, New York, 1949.
- [2] J. Roskam. *Airplane Flight Dynamics And Automatic Flight Controls - Part I*. Darcorporation.
- [3] R. D. Finck. *USAF Stability and Control DATCOM*. AFWAL-TR 83-3048, McDonnell Douglas Corporation, Wright-Patterson Air Force Base, Ohio, 1978.
- [4] P. Della Vecchia, F. Nicolosi and D. Ciliberti. *Aircraft directional stability prediction method by CFD*. In 33rd AIAA Applied Aerodynamics Conference, 2015.
- [5] S. Corcione. *Design guidelines, Experimental Investigation and Numerical Analysis of a New Twin Engine Commuter Aircraft*. Ph.D. thesis, Università degli Studi di Napoli “Federico II”, 2015.
- [6] J. B. Barlow, W. H. Rae, and A. Pope. *Low-speed wind tunnel testing*. Wiley, New York, 3rd edition, 1999.

ACKNOWLEDGEMENT/RINGRAZIAMENTI

Ci tengo a ringraziare:

- Il prof Fabrizio Nicolosi per l'opportunità di crescita che mi ha concesso grazie a questo lavoro sperimentale dal grande interesse scientifico e tecnico.
- Il mio correlatore, l'ing. Danilo Ciliberti, per aver condiviso con me la sua esperienza sperimentale ma, soprattutto, per il suo continuo supporto morale e didattico durante tutto il lavoro svolto.
- Gli ingegneri Salvatore Corcione, Pierluigi Della Vecchia e Vincenzo per i preziosi consigli e per l'aiuto fornitoci durante le prove in galleria.
- Il tecnico di laboratorio, Antonio, per la sua preziosa esperienza e continua disponibilità.

Nicola